Structural Insights into Kainate Receptor Desensitization

Changping Zhou[1,2], Guadalupe Segura-Covarrubias[1,2], and Nami Tajima[✓1]

[1] Department of Physiology and Biophysics, Case Western Reserve University School of Medicine, Ohio, 44106, USA.

[2]Equal contribution

[✓]Correspondence to nxt193@case.edu (N.T.)

Highlights

1. We present cryo-EM structures of GluK2 kainate receptors with engineered cysteine crosslinks at the inter-dimer interface, which restrict subunit lateral rotation and attenuate receptor desensitization.
2. The structure of GluK2 double cysteine mutant in complex with the allosteric potentiator BPAM344 and glutamate represents a non-desensitized state, highlighting the critical conformational changes required for ion channel gating.
3. The glutamate-bound GluK2 mutant adopts multiple conformations, representing both shallow- and deep-desensitized states. Electrophysiological recordings indicate that the GluK2 kainate receptor mutant recovers from desensitization more rapidly, resembling AMPA receptors. Our structural and functional data suggest that shallow-desensitized KARs remain conductive, implying that the large lateral LBD rotation during KAR desensitization is essential for complete channel closure, distinguishing KARs from other iGluRs.

Keywords

Kainate-type ionotropic glutamate receptors; structure; desensitization mechanism.

Abstract

Kainate receptors (KARs), along with AMPA and NMDA receptors, belong to the ionotropic glutamate receptor (iGluR) family and play critical roles in mediating excitatory neurotransmission throughout the central nervous system. KARs also regulate neurotransmitter release and modulate neuronal excitability and plasticity. Receptor desensitization plays a critical role in modulating the strength of synaptic transmission and synaptic plasticity. While KARs share overall structural similarity with AMPA receptors, the desensitized state of KARs differs strikingly from that of other iGluRs. Despite extensive studies on KARs, a fundamental question remains unsolved: why do KARs require large conformational changes upon desensitization, unlike other iGluRs? To address this, we present cryo-electron microscopy structures of GluK2 with double cysteine mutations in non-desensitized, shallow-desensitized and deep-desensitized conformations. In the shallow-desensitized conformation, two cysteine crosslinks stabilize the receptors in a conformation that resembles the desensitized state of AMPA receptors. However, unlike the tightly closed pore observed in the deep-desensitized KAR and desensitized AMPAR conformations, the channel pore in the shallow-desensitized state remains incompletely closed. Patch-clamp recordings and fluctuation analysis suggest that this state remains ion-permeable, indicating that the lateral rotational movement of KAR ligand-binding domains (LBDs) is critical for complete channel closure and stabilization of the receptor in desensitization states. Together with the multiple conformations representing different degree of desensitization, our results define the unique mechanism and conformational dynamics of KAR desensitization.

50 **Main**

51 Kainate receptors (KARs) belongs to the ionotropic glutamate receptor (iGluR) superfamily
52 together with α-amino-3-hydroxy-5-methyl-4-isoxazolepropionic acid (AMPA), *N*-methyl-d-
53 aspartate (NMDA) and delta receptors. They are cation selective ligand-gated ion channels
54 activated by an excitatory neurotransmitter glutamate and mediate fast excitatory synaptic
55 transmission in mammalian brains[1,2]. In addition to their role in mediating the synaptic
56 transmission at post-synapses, KARs also function pre- and extra-synaptically, and regulate
57 excitatory and inhibitory neurotransmitter release and modulate synaptic excitability[3-7]. Abnormal
58 expression and dysfunction of KARs are associated with various neurological diseases and
59 disorders, including schizophrenia, mood disorders, epilepsy, and Huntington's disease[8-17].
60 Therefore, KARs are considered potential therapeutic drug targets due to their physiological and
61 pathophysiological roles[18-21].

62 Kainate receptors (KARs) assemble as homo- or heterotetramers composed of five
63 subunits: GluK1–5[22-25]. Extensive studies revealed that KARs adopt a Y-shaped architecture with
64 four distinct layers: the amino-terminal domain (ATD), which is critical for receptor assembly; the
65 ligand-binding domain (LBD), which contains ligand-binding sites and regulates channel gating;
66 the transmembrane domain (TMD), which forms the ion channel within the plasma membrane;
67 and a short disordered C-terminal domain (CTD), which interacts with intracellular proteins[1,26].
68 Recently determined structures of intact KARs in various liganded states have elucidated the
69 structure-function correlations underlying the mechanisms of activation/desensitization[25,27-31],
70 allosteric modulation[32], inhibition[33], and channel block[34]. A characteristic structural feature of
71 KARs lies in their unique conformation during desensitization. Structures of intact GluK2, first
72 reported in 2014 by the Mayer/Subramaniam lab, have indicated that KAR LBD dimer assemblies
73 are completely dissociated upon desensitization, with a large horizontal-plane rigid-body rotation
74 of the LBDs in the BD subunits, resulting in an approximately four-fold symmetric structures, while

75 other iGluRs typically retain two-fold symmetric conformations viewed from the top when they are
76 desensitized[26,28]. In addition, a key functional characteristic of KARs is their significantly slower
77 recovery from desensitization — over 50 fold slower compared to AMPARs[35,36]— which limits KAR
78 mediated rapid and high-frequency transmission in neurons[37]. Due to the rapid onset of
79 desensitization induced by the neurotransmitter glutamate, which closes the ion channel within a
80 few milliseconds, previous KAR structures in complex with glutamate have been stabilized in fully
81 or deep-desensitized states, with the ion channel fully closed[25,27-31,33,38-40]. Despite their unique
82 structural and functional features, why only KARs exhibit such a strikingly different conformation,
83 which is not conserved in other iGluRs, and how these drastic conformational changes control
84 receptor gating remains elusive.

85 To address this outstanding question, we present the cryo-electron microscopy (cryo-EM)
86 structure of the GluK2 KAR in multiple functional states, including non-desensitized, shallow-
87 desensitized, intermediate (between shallow and deep desensitized), and deep-desensitized
88 conformations, using cysteine cross-linking in the presence of glutamate and the positive
89 allosteric modulator BPAM344. The structural comparison revealed that the large in-plane rotation
90 of LBDs in both BD subunits and the resulting twisted motion of the LBD-TM3 linkers are essential
91 for tight ion channel closure and stabilization of receptors in the deep-desensitized state—a
92 feature not observed in AMPARs and NMDARs. Functionally, the crosslinked GluK2 mutant
93 exhibits large fractional steady-state currents, as revealed by patch-clamp recording. The
94 stationary noise analysis results indicate that the GluK2 mutant remains conductive when
95 desensitized, resembling the behavior of the conductive GluA2(R) AMPAR under similar
96 conditions[41]. These structural and functional results show that robust in-plane rotations of the
97 LBDs are essential for proper ion channel closure. Overall, our study provides new insights into
98 the unique desensitization mechanism of the KAR subfamily.

99

Results

Trapping GluK2 KARs in a non-desensitizing state

Previous studies have shown that LBD dimer reorientations switch the gating of KARs[27-29]. To gain insight into the detailed conformational transitions from active to desensitized states, we first generated a homology model of the intact open GluK2 receptor, comprising the ATD, LBD, and TMD layers based on the structure of the activated GluA2 AMPA receptor in the presence of glutamate, potentiator, and auxiliary subunit in its higher conductive open state (Protein Data Bank (PDB) code 5WEO)[42-44] using SWISS-MODEL[45-49] (Fig. S1A, B). In the model, the G/E helices of subunit A and the K helix of subunit B come into close proximity (Fig. S1C, D), resembling the recently determined structure of GluK2 bound to glutamate, an allosteric positive modulator BPAM344, and Concanavalin A (ConA) in an open state, using time-resolved cryo-EM (PDB code 9B36)[27]. Specifically, the distances between the Cα atoms of K676 in subunit A and N802 in subunit B are 6.2 Å and 6.7 Å in the homology model and the active/open GluK2 structure, respectively. By contrast, these distances are much greater in the BAPM344-bound (no agonist supplemented) inactive state (PDB code 8FWS)[32], as well as in the antagonized (PDB code 5KUH)[28], and desensitized (PDB code 9B38, 5KUF)[27,28] states (Fig. S1D). Cysteine crosslinking approaches have been used to analyze the dynamics and the channel function of iGluRs[50-54]. Additionally, a recent report showed that the conformational changes of KARs upon activation resembles those of AMPARs[27]. Based on these reports, we hypothesized that an engineered disulfide bond between residues K676 and N802 would restrict the mobility of the LBD and trap a dimer-of-dimers LBD conformation, potentially altering desensitization kinetics. To test this hypothesis, we introduced a pair of cysteine residues designed to form disulfide bonds between the LBD dimer pairs (Fig. S1 E, F) and assessed the channel activity of the full-length rat GluK2 K676C/N802C mutant using whole-cell patch-clamp recordings. Note that the distance between the Cα atoms of two cysteines required to form a disulfide bond is reported to be less than 7 Å[55].

125 GluK2 wild type (WT) demonstrated the rapid desensitization, as observed previously[35].
126 By contrast, the GluK2 K676C/N802C mutant, activated by 1 mM glutamate, showed earlier rapid
127 desensitization and a steady-state current (Fig. 1A). When we assessed the GluK2 K676C and
128 GluK2 N802C single cysteine mutants, both exhibited nearly complete desensitization, similar to
129 GluK2 WT, without displaying the steady-state current observed when the GluK2 K676C/N802C
130 double cysteine mutant was activated by glutamate (Fig. S2A). These results confirm that disulfide
131 bond formation between K676C and N802C are responsible for generating the steady-state
132 current.

133 An earlier study showed that BPAM344 significantly slows the desensitization kinetics of
134 GluK2 WT and enhances the glutamate-evoked current by 140-fold and 21-fold, respectively[56].
135 To assess how BPAM344 modulates the activation and desensitization of the GluK2
136 K676C/N802C mutant, we next analyzed its effect. Indeed, the percent desensitization of GluK2
137 K676C/N802C elicited by 1 mM glutamate is dramatically decreased in the presence of 0.5 mM
138 BPAM344, with only 25% desensitization observed after 20 seconds (Fig. 1 A, B). While the peak
139 current amplitude (I_{peak}) was increased 1.5-fold (1.5 ± 0.3, n=10), similar to the WT in the presence
140 of BPAM344, the steady-state current (I_{ss}) amplitudes were also significantly increased, by
141 approximately 4.7-fold (4.7 ± 0.6, n=10) (Fig. 1C). Thus, we sought to capture the conformation
142 of receptors in this non-desensitizing state using cryo-EM.

143

144 **GluK2 K676C/N802C adopts multiple conformations**

145 We expressed the intact homotetrameric GluK2 KAR incorporating K676C/N802C double
146 cysteine mutations in HEK293S GnTI$^-$ cells and purified the proteins in the detergent, n-Dodecyl-
147 B-D-Maltoside (DDM). The final protein sample (Fig. S2B, C) was pre-incubated with 1 mM
148 glutamate, with or without 0.5 mM BPAM344, prior to grid freezing. We initially performed 3-
149 dimensional (3D) refinement without imposing symmetry (Table S1). Our initial global

150 reconstruction of the glutamate/BPAM344-supplemented dataset generated six main classes (Fig.
151 S3a). One of the classes has a two-fold rotational symmetrical conformation (Fig. 1D), with the
152 extracellular domains resembling the open-state conformation (PDB code 9B36)[27]. To improve
153 the density, we further performed signal subtraction on the ATD and LBD-TMD layers separately.
154 The local refinements with focused masks yielded 3.7 Å and 3.9 Å reconstruction of the ATD and
155 LBD-TMD, respectively, enabling reliable model building (Fig. S3a, S4 A–C). The reconstruction
156 of the LBD-TMD showed clear density for BPAM344 at the LBD dimer interface consistent with
157 previous reports[27,32,57] (Fig. 1E–G). All four LBD bi-lobes are closed in the presence of glutamate,
158 compared to its open conformation in an apo GluK2 (PBD code 9CAZ) structure (Fig. 1H, I). While
159 the extracellular domain adopts an active-like conformation, the ion channel pore remains closed.
160 Therefore, we refer to this class as a non-desensitized conformation.

161 In contrast, the remaining five classes showed no BPAM344 molecules at the LBD D1-D1
162 interface, leading to D1-D1 rupture. In all of these five classes, the LBD bi-lobes of all four subunits
163 are tightly closed in the presence of glutamate, with closure degrees ranging from 23° to 27°,
164 indicating glutamate binding to the receptors. The overall structures of these five conformations
165 are stabilized in two- or four-fold symmetrical, or asymmetrical arrangements. In order to analyze
166 conformations in the absence of allosteric potentiators, we also collected cryo-EM data of GluK2
167 K676C/N802C supplemented with glutamate. These data revealed four main three-dimensional
168 (3D) classes (Fig. S3b), each are superimposable with the glutamate-bound, BPAM344-unbound
169 classes from the BPAM344-supplemented sample (Fig. S3a). Thus, we combined these two data
170 sets and further performed processing and refinement to improve the density quality. We defined
171 these classes as shallow-desensitized, intermediate, and deep-desensitized states, based on the
172 observations described below. Ultimately, the final resolutions of desensitized classes range from
173 3.7 Å to 4.0 Å (Fig. S4).

174

175 **GluK2 K676C/N802C mutant structure bound to glutamate and BPAM344 represents a non-**
176 **desensitized conformation**

177 While all six 3D reconstructions showed three domains—ATD, LBD, and TMD—as
178 previously reported[25,28,30,31,33], each class showed distinct conformations (Fig. S3). In the non-
179 desensitized structure, two molecules of BPAM344 per LBD dimer bind and stabilize the LBD D1-
180 D1 interfaces, with each BPAM344 forming hydrogen bonds with the side chain of P532, as
181 recently reported[27,32,57] (Fig. 1G). In addition to BPAM344, clear densities corresponding to
182 disulfide bonds between K676C and N802C were observed in this conformation (Fig. 1J). These
183 two disulfide bonds trapped the LBDs in a dimer-of-dimers conformation in the presence of the
184 agonist, as designed (Fig. 1D, F). Previously, the structure of open GluK2 was determined in the
185 presence of two positive allosteric modulators, concanavalin A (ConA), BPAM344, as well as the
186 agonist glutamate (PDB code 9B36)[27]. In the structure, the ~50 kDa ConA dimer, along with
187 BPAM344 and glutamate, binds at the ATD-LBD interface, elevating the ATD by 16 Å and rotating
188 the LBD relative to the ATD layer by 28° (Fig. S5). The same tendency was observed in the
189 presence of NETO auxiliary proteins, which also bind to the ATD and LBD layers and modulate
190 KAR kinetics[30]. Interestingly, a comparison between structures without an orthosteric ligand (PDB
191 codes 8FWQ, 9CAZ)[32] and our non-desensitized structure revealed that the distance between the
192 center of mass (COM) of the ATD and LBD was also increased by 7.5 Å in the non-desensitized
193 conformation, even in the absence of ConA and NETO auxiliary proteins. By contrast, in the
194 desensitized state, this distance between the ATD and LBD decreased by 2–4 Å compared to the
195 apo state. While, the ATDs in all structures are superimposable and do not undergo any
196 conformational changes (Fig. S5B), the ATD in the non-desensitized class also displayed a rigid-
197 body rotation of 45° counterclockwise (Fig. S5C), following the same movement tendency
198 observed in the open state of KARs[27] and AMPARs[58].

199 Focusing on the LBD layer, the LBDs are stabilized in a dimer-of-dimers arrangement that
200 resembles the open conformation (Fig. 2A), with the D1–D1 association stabilized by BPAM344
201 and the D2–D2 separation maintained within each LBD dimer in the presence of glutamate (Fig.
202 2B). Analysis of the center-of-mass (COM) distances between D1-D1 and D2-D2 in the two
203 structures further indicates their similar conformational arrangement. Specifically, the distance
204 between the Cα atoms of S670, located at the bottom of the D2 lobes in the AD and BC subunit
205 pairs, is equally separated as seen in the open-state conformation. Key features of the open-state
206 conformation of iGluRs include increased tension in LBD-TM3 linkers and the expansion of the
207 ion channel pore held by the linkers, particularly at the gate region[1,59]. Thus, we next compared
208 the LBD-TM3 linker arrangement, TM3 helix orientation, and channel openings in the BPAM344-
209 bound (without an orthosteric ligand), non-desensitized, and open GluK2 conformations. The
210 densities of all TM3 helices are well resolved (Fig. S6). In the non-desensitized conformation, the
211 TM3 helices are unwound at A656 in the BD subunits and at E662 in the AC subunits (position
212 (3) and (2'), respectively), and therefore, T660 (BD subunits) and M664 (AC subunits) are pulled
213 away from the ion channel central axis, while BPAM344-bound GluK2 (PDB code 8FWS)[32]
214 displays an additional half-turn of the helix at the pore entrance, and the TM3 helices unwind at
215 T660 in the AC subunits and at M664 in the BD subunits (position (2) and (1), respectively) (Fig.
216 2C). Consequently, the top of the gating region, which contains the conserved SYTANLAAF
217 motif[60,61], is more dilated in the non-desensitized conformation compared to the more tightly
218 closed BPAM344-bound GluK2 conformation. By contrast, the TM3 helices in the open GluK2
219 conformation (PDB code 9B36)[27] display kinking at a deeper position, specifically at L655
220 (position (4)) in all four subunits (Fig. 2D). Additionally, the open GluK2 conformation exhibits the
221 rotational movements of TM3, which put away T652 from the central axis of the pore, thus opening
222 the channel. However, these rotational movements are not observed in the non-desensitized
223 conformation. Overall, the ion channel in the non-desensitized conformation remains closed (Fig.
224 2E, F).

225

226 **Disulfide bonds between K676C-N802C stabilized GluK2 KARs in a desensitized AMPA**
227 **receptor like conformation**

228 The glutamate-bound, potentiator-unbound GluK2 K676C/N802C generated five classes
229 (Fig. 3A). The LBD layer conformations in these classes appear desensitized; however, they
230 represent different levels of desensitization (Fig. 3B). In one of these desensitized classes, the
231 absence of BPAM344 results in D1–D1 dissociation, a hallmark structural feature of iGluR
232 desensitization, while two disulfide bonds between K676C and N802C (Fig. 3C) stabilize LBD
233 dimers forming a dimer-of-dimers conformation. We refer to this as the 'shallow-desensitized'
234 conformation to distinguish it from the typical deep-desensitized conformations previously
235 observed[28]. Another class, termed the intermediate state, contains an LBD dimer on one side and
236 a disrupted dimer on the other. In this class, one LBD dimer pair maintains its dimer formation
237 with D1–D1 dissociation, resembling the shallow-desensitized state, while the disrupted dimer
238 adopts a conformation characteristic of deep-desensitized classes. Therefore, we propose that
239 this structure represents an intermediate state between the shallow- and deep-desensitized
240 conformations in the presence of glutamate. In contrast, the other three structures lacked inter-
241 subunit disulfide bonds between K676C and N802C, resulting in the LBD layers stabilizing an
242 approximately four-fold symmetric conformation, though with varying in-plane rotation angles of
243 the LBDs (Fig. 3B). We observed the formation of a 'desensitization ring' (Fig. 3D, E) in all three
244 deep-desensitized conformations, consistent with previous reports[28,29,62]. This ring formation plays
245 a key role in regulating desensitization and recovery from desensitization[28,29]. Accordingly, we
246 classified these classes as 'deep-desensitized' states."

247 Comparison of the non-desensitized and shallow-desensitized conformations reveals
248 multiple structural rearrangements in the context of the full-length receptor structure. The distance
249 between the ATD and LBD decreases in the shallow-desensitized state, measuring 2–3 Å shorter

250 than in the apo and BPAM-bound GluK2 structures, making it more similar to the deep-
251 desensitized state than to the open-state conformation (Fig. S5A). Focusing on the LBD layer,
252 the LBDs in the AC subunits are rotated by 5° parallel to the membrane when viewed from the
253 top, compared to the non-desensitized conformation (Fig. 4A). Viewed from the side, the entire
254 LBDs appear rolled down (Fig. 4B), which is associated with the rearrangement of the dimer-of-
255 dimers formation and the rupture of the D1-D1 interface. These conformational changes are also
256 observed during AMPAR desensitization[44,63-66]. Therefore, we next compared the shallow-
257 desensitized conformation of GluK2 K676C/N802C with the desensitized conformation of GluA2
258 AMPAR (PDB code 7RYZ)[64]. Viewed from the top, the distance between the Cα atoms of S700
259 (S662 in GluA2 AMPAR) in both structures are reduced compared to their respective open states,
260 although the arrangements in these two structures differ due to the restricted mobility of GluK2
261 caused by cysteine crosslinks (Fig. 4C). The D1 lobes of GluK2 roll down approximately 25°, in
262 contrast to the 33° rolling-down motion observed in the D1 lobes of GluA2 (Fig. 4D). The D2
263 distances in the shallow-desensitized GluK2 and desensitized GluA2 are comparable, measuring
264 20 Å and 24 Å, respectively. Overall, the shallow-desensitized conformation of the GluK2 mutant
265 appears to resemble the desensitized conformation of AMPA receptors. However, this
266 conformation in KAR is energetically unstable and has not been observed in the absence of
267 crosslinks. Comparison of the TM3 in the non-desensitized and shallow-desensitized
268 conformations revealed that the pore in the shallow-desensitized state is occluded at T660, and
269 M664 in the BD and AC subunits, respectively (position (2) and (1)) (Fig. 4E), while the ion channel
270 pore in the deep-desensitized conformations is sealed at M664 (position (1)) in all four subunits
271 (Fig. 4F).

272

273 **A large in-plane rotation of the LBD is required for proper ion channel closure during**
274 **desensitization in GluK2 KAR.**

275 We next assessed the ion channel pore in these desensitized conformations. Although the
276 extracellular domain in the shallow-desensitized GluK2 KAR and the desensitized GluA2 AMPAR
277 adopt similar conformations, we observed distinct differences in their ion channel pore structures
278 (Fig. 5A–C). The shallow-desensitized conformation has restriction points around T652, A656,
279 and T660, which correspond to T617, A621, and T625 in the desensitized GluA2 (PDB code
280 7RYZ)[64]. Notably, the pore diameter at T660 and T652 in the shallow desensitized GluK2 KAR is
281 wider compared to that in the desensitized GluA2 AMPAR. The ion channel pore in the transition
282 state is also similar to that in the shallow-desensitized state, except for the presence of a narrower
283 restriction point (<1 Å) around T652 (Fig. 5A). By contrast, all three deep-desensitized
284 conformations exhibit multiple tight constrictions, particularly at the top of the gate region (Fig. 5A,
285 D).

286 As previously reported[28,29], the 'desensitization ring' at the bottom of the LBD layer in these
287 deep-desensitized conformations is stabilized by numerous polar interactions, supporting the
288 four-fold symmetrical deep-desensitized conformations, whereas the shallow-desensitized and
289 intermediate conformations exhibit disrupted ring formation, resulting in wider gate regions.
290 Moreover, the large in-plane rotation of the LBDs in the BD subunits during desensitization twists
291 the LBD-TM3 linker, creating an additional constriction at M664 at the top of the channel pore
292 (Fig. 4F), which is not seen in AMPARs. We observe that the formation of the desensitization ring
293 at the bottom of the LBD layer tightly closes the ion channel in the deep-desensitized
294 conformations, whereas the shallow-desensitized state lacks this secure channel pore lock at
295 T660 and M664 (Fig. 5A).

296 Based on these functional and structural observations, we hypothesized that the GluK2
297 KAR K676C/N802C mutant, which forms cysteine crosslinks, undergoes shallow rather than deep
298 desensitization. This may allow the receptors to remain ion-permeable, exhibit a higher open

299 probability, or recover quickly from desensitization, similar to AMPARs, thereby enabling more
300 efficient activation of the receptors.

301

302 **K676C-N802C cysteine crosslinks partially blocks receptors from undergoing deep**
303 **desensitization**

304 To test our hypothesis, we first assessed the kinetics of the GluK2 K676C/N802C mutant
305 using whole-cell patch-clamp electrophysiology. Remarkably, we observed steady-state currents
306 of the cross-link mutant even at the highest concentration of glutamate (50 mM), which were not
307 observed in the wild type GluK2 receptors (Fig. 6A). There were no significant differences neither
308 in the current density at peak current between GluK2 WT and the mutant (GluK2 WT: 830 ± 50
309 pA/pF, n=6; GluK2 K676C/N802C: 700 ± 150 pA/pF, n=9), nor in the EC_{50} for glutamate (GluK2
310 WT: 110 ± 30 μM, n=7; GluK2 K676C/N802C: 150 ± 50 μM, n=5), indicating that the cysteine
311 crosslinks do not significantly affect agonist binding affinity or receptor activation (Fig. 6A-D).
312 GluK2 K676C/N802C partially desensitized even by 0.01 mM glutamate, a concentration below
313 the EC_{50} (approximately 0.17 mM). This suggests that even partial occupancy is sufficient to
314 initiate the conformational changes leading to desensitization, consistent with earlier findings[67,68].
315 While GluK2 WT desensitizes almost completely with a time constant of 8 ± 1 ms (n=14), the
316 GluK2 K676C/N802C receptors in the presence of 0.01–50 mM glutamate exhibited
317 approximately 60% desensitization, except when activated by 0.001 mM glutamate where only
318 the steady-state current was observed with a decreased peak amplitude (Fig. 6E). Therefore, the
319 degree of desensitization is not glutamate concentration dependent.

320 To assess the desensitization state of the crosslinked mutant, we next analyzed the rate
321 of recovery from desensitization. As previously reported, recovery from desensitization in the
322 GluK2 WT is extremely slow, requiring 1,150 ± 90 ms (n = 9) for full recovery. By contrast, the
323 GluK2 K676C/N802C mutant exhibited a faster recovery from desensitization, characterized by

324 two distinct components: τ_1 (100 ms, 60%) and τ_2 (1,000 ms, 40%) (n = 9). The τ mean of the
325 mutant was 440 ± 40 ms, approximately three times faster than that of GluK2 WT (Fig. 6F–H).
326 This shift brings its kinetics closer to those of AMPARs, which recover in the order of tens to
327 hundreds of milliseconds (e.g. GluA1 and GluA2 wild-type recovery constants are approximately
328 200 ms and 9-50 ms, respectively)[69-71]. This result highlights the impact of cysteine cross-linking
329 in accelerating desensitization recovery, potentially by stabilizing the dimer-of-dimers
330 conformation.

331

332 **GluK2 KAR stabilized in a shallow-desensitized conformation remains ion-permeable**

333 To assess whether the non-desensitized current and faster recovery kinetics result from
334 crosslinking between the K676C and N802C, we performed whole-cell recordings in the presence
335 of 5 mM dithiothreitol (DTT), applied for 7 minutes prior to the second glutamate activation. The
336 peak intensity of both GluK2 WT and GluK2 K676C/N802C, in the presence and absence of DTT,
337 showed no significant changes, confirming our earlier analysis that the crosslinks do not affect
338 activation kinetics (Fig. 7A). By contrast, the application of 5 mM DTT for 7 minutes led to a >90%
339 reduction in the steady-state current of GluK2 K676C/N802C (steady-state current prior to and
340 after DTT application: 0.4 ± 0.1 nA and DTT: 0.03 ± 0.03 nA, respectively, n=8) (Fig. 7B).
341 Additionally, recovery from desensitization of the DTT treated cells expressing GluK2
342 K676C/N802C was 1,040 ms ± 50 (n=5), similar to the WT (Fig. 7C, D). This experiment, together
343 with the assessment of the single cysteine mutants, GluK2 K676C and GluK2 N802C (Fig. S2A),
344 confirms that the observed non-desensitizing efficacy is specifically due to disulfide bond
345 formation, which stabilizes the two-fold symmetrical non-desensitized or shallow-desensitized
346 conformations as originally intended.

347 Next, we aimed to determine whether crosslinked receptors remain ion-conductive when
348 exhibiting steady-state current. A key feature of KARs is their exceptionally small conductance

349 and low open-channel probability, which makes it technically challenging to directly observe
350 channel activity at the single-channel level, unlike other channels, including AMPARs[72,73].
351 Therefore, we conducted noise analysis to assess its conductivity. We first performed
352 nonstationary fluctuation analysis (NSFA) on the desensitizing phase of macroscopic currents
353 from GluK2 WT and GluK2 K676C/N802C, activated by glutamate pulses (10 mM, 100 ms). The
354 variance of fluctuations around the expected current was analyzed. The weighted mean single-
355 channel conductance of GluK2 WT was calculated as 23 ± 7.8 pS (n = 5), consistent with previous
356 report[72]. While the current-variance relationship of the wild type was well-fitted by a parabolic
357 function, the analysis of GluK2 K676C/N802C revealed an anomalous current-variance
358 relationship, preventing the calculation of its conductance (Fig. 7E). However, the mutant
359 generates a unique large fractional steady-state current. Thus, we next analyzed stationary
360 fluctuation on the steady-state current of the desensitized receptors in the presence and absence
361 of BPAM344.

362 To assess unitary conductance and the number of active channels, we analyzed the
363 microscopic currents of GluK2 K676C/N802C activated by 10 mM glutamate for 30 seconds under
364 desensitizing conditions (Fig. 7F). When activated by 10 mM glutamate, the mutant exhibited a
365 unitary conductance of 10 pS—less than half of the wild-type conductance calculated by NSFA—
366 and was similar to the lowest conductive level (O1) previously determined for KARs[72]. Variance-
367 current analysis across individual cells showed that BPAM344 shifted receptor behavior toward
368 higher variance and mean current values (Fig. 7G), suggesting an increase in the number of open
369 receptors and their open probability. Interestingly, the conductance of the mutant activated by 10
370 mM glutamate was similar in the presence and absence of BPAM344 (GluK2 K676C/N802C, 10
371 mM glutamate: 10 ± 3 pS, n = 6; GluK2 K676C/N802C, 10 mM glutamate + 0.5 mM BPAM344:
372 10 ± 2 pS, n = 6) (Fig. 7H). Whereas the number of active channels in the presence of BPAM344
373 was approximately four-fold higher than in its absence (GluK2 K676C/N802C, 10 mM glutamate:

374 1,040 ± 600, n = 6; GluK2 K676C/N802C, 10 mM glutamate + 0.5 mM BPAM344: 4,080 ± 460, n
375 = 6) (Fig. 7I). In summary, these experiments indicate that desensitized GluK2 K676C/N802C
376 KARs remain conductive at the single channel level, although with significantly lower conductance
377 compared to wild-type channels activated by glutamate.

378

379 **Discussion**

380 Receptor desensitization is a fundamental property of ligand-gated ion channels which
381 depends on agonist, receptor subtypes, and auxiliary proteins. Recent advances in iGluR
382 research have revealed significant differences in the kinetics and conformational dynamics of
383 KARs during desensitization compared to other iGluRs[1,25,28,29,31,33]. The desensitized conformation
384 of KARs is characterized by the quasi-four-fold symmetrical LBDs, by contrast to typical
385 desensitized iGluRs, which remain in two-fold symmetrical conformations. In addition, functionally,
386 the majority of KARs enter deep-desensitized states, with recovery from desensitization occurring
387 5- to 130-fold slower than AMPARs. By contrast, most AMPARs typically adopt shallow-
388 desensitized states, exhibiting deep desensitization only under certain conditions[74,75]. In this study,
389 we employed a classical cysteine crosslinking approach to answer the fundamental question why
390 KARs require such dramatical conformational changes for proper channel closure and complete
391 desensitization, which are not conserved in other iGluRs.

392 In the previously determined structure of BPAM344- and ConA-bound GluK2 in a highly
393 ion-conductive open state, ConA binds both the ATD and LBD, occupying the space between
394 these two layers[27]. As a result, the organization of the ATD-LBD layers upon activation remains
395 unclear. In this study, we analyzed the extracellular domain organization in the absence of ConA.
396 The assembly of the extracellular domains of our glutamate- and BPAM344-bound GluK2
397 K676C/N802C in the non-desensitized state resembles that of GluK2 in its open state.
398 Interestingly, in the absence of ConA, the ATD-LBD distance in the non-desensitized state of

399 GluK2 K676C/N802C is wider. Thus, upon activation, the ATD layer is elevated and undergoes a
400 counterclockwise in-plane rotation. By contrast, the apo and desensitized receptors adopt more
401 compact extracellular domain conformations, with ATD and LBD layers positioned closer. Since
402 ATD-deleted KARs remain functional as ion channels[27,76], further investigation is needed to
403 determine how these conformational changes in the ATD layer contribute to receptor activation.
404 In addition, we also observed the TM3, which form the gating region of the ion channel pore, kinks
405 at the position between the kinking observed in the apo and the open structure (Fig. 8), along with
406 rotational movement of TM3. This observation suggests that TM3 kinking at a higher position
407 (A656/E662) within the gating region is insufficient for channel opening—particularly full opening
408 with high conductivity—which instead requires TM3 rotation and kinking at a lower position (L655)
409 in all four subunits (Fig. 8).

410 Conversely, the glutamate-bound GluK2 K676C/N802C structures represent shallow- and
411 deep- desensitized conformations as well as an intermediate state between these two
412 desensitized states. The shallow-desensitized conformation demonstrates that two inter-dimer
413 crosslinks stabilize receptors in a two-fold symmetrical conformation with D1-D1 ruptured LBDs,
414 similar to the desensitized state of AMPARs[42,44,63-65]. While most previously determined AMPAR
415 structures in desensitized states are stabilized in the classical two-fold symmetrical conformation,
416 the partial agonist, fluorowilliardiine-bound GluA2 AMPAR, in a desensitized state exhibited an
417 asymmetrical conformation with the LBD of subunit D undergoing a large conformational
418 rearrangement similar to our GluK2 in the intermediate-state conformation[77]. Additionally, recent
419 studies have shown that extracellular protons influence extracellular domains and alter LBD
420 conformation, causing minor in-plane rotation of LBDs within the submit B and D, although these
421 changes are not as pronounced as those observed in the deep-desensitized KAR
422 conformations[70,71,78]. Nevertheless, adopting the four-fold symmetrical deep-desensitized
423 conformation is not energetically favorable for AMPARs during desensitization[74], whereas KARs

424 exhibit greater stability in this four-fold conformation. Previous mutagenesis studies demonstrated
425 that various mutations in the D2 lobe of KARs alter desensitization and recovery from
426 desensitization, but no mutation completely blocked desensitization unlike AMPARs[62]. This
427 suggests that multiple non-conserved residues contribute to the stability of the four-fold
428 desensitized conformation of KARs, despite the overall architectural similarity between AMPAR
429 and KAR LBDs. Our electrophysiological experiments demonstrate that cysteine crosslinking
430 prevents the receptors from undergoing complete desensitization, resulting in significantly
431 stronger and faster recovery—resembling the kinetics of AMPARs rather than those of GluK2 WT.
432 Upon treatment with 5 mM DTT, which breaks the disulfide bonds in the GluK2 K676C/N802C
433 mutant, recovery from desensitization resembled that of the WT, indicating a correlation between
434 LBD conformation and desensitization recovery in GluK2 KAR.

435 Furthermore, we aimed to understand why KARs have to form the four-fold symmetrical
436 arrangement upon desensitization. Previous studies have shown that in the "desensitized ring", a
437 network of polar interactions stabilizes the deep-desensitized conformation of the LBD layer. This,
438 in turn, helps to stabilize the conformation of the TMD layer, thereby reinforcing receptor
439 desensitization and influencing the kinetics of desensitization recovery[28,29]. In the shallow-
440 desensitized conformation, lacking desensitization ring formation with the two-fold symmetric
441 LBDs, we observed that the ion-channel is dilated by contrast to channels observed in
442 desensitized AMPARs and fully/deep desensitized KARs, which show much narrower channel
443 pores throughout the gating region with the channel pore tightly sealed on the top of the gating
444 region. Previously, a conducting desensitized state of AMPAR and acetylcholine receptors has
445 been reported[41,79]. In addition, it was microscopically shown that the partially desensitized KARs
446 are conductive, as defined by the number of desensitized subunits per KAR tetramer[80]. The
447 structural observation together with the characteristic steady-state current of the GluK2
448 K676C/N802C indicates that the receptors in the shallow-desensitized state could form weakly

449 conductive channels. Indeed, our noise analysis demonstrates that the desensitized GluK2
450 K676C/N802C receptors, exhibiting steady-state current, remains conductive at the single-
451 channel level; however, its conductance is approximately 30% weaker than the GluK2 WT,
452 regardless of the presence of the positive allosteric modulator BPAM344. In addition, the
453 crosslinked receptors exhibit up to ten-fold faster recovery from desensitization, whereas reducing
454 the disulfide bonds with DTT restores currents similar to those of the GluK2 WT.

455 Taken together, this study answers the fundamental question by demonstrating that KARs
456 absolutely require large conformational rearrangements of the LBD layer and stabilization in a
457 four-fold symmetrical conformation to achieve proper channel closure and full desensitization into
458 a non-conductive state (Fig. 8). This structural feature distinguishes KARs from other iGluR
459 subfamilies, in which such symmetry and conformational changes are not observed.

460

461 **Materials and Methods**

462 **Plasmid construction**

463 For Cryo-EM studies, the construct used for the structural studies was full-length rat GluK2 KAR
464 (GenBank 54257, Uniprot code P42260) with two mutations of N802C and K656C. The gene was
465 cloned into the pFW vector (gift from Dr. Hiro Furukawa at Cold Spring Harbor Laboratory) and
466 fused to a C-terminal human rhinovirus 3C protease recognition site and a 1D4 affinity tag. The
467 construct was referred to as GluK2 N802C/K656C.

468

469 **Cell culture**

470 For structural studies, HEK293S GnTI$^-$ cells were grown to a density of 3.2×10^6 cells / ml
471 in FreeStyle 293 medium at 37°C and 8% CO_2 supplemented with 2 % fetal bovine serum. The
472 rGluK2 N802C/K676C mutant bacmid and baculovirus were generated as previously described.
473 The P1 and P2 viruses were produced in Sf9 cells. Cells were infected with the baculovirus

474 harboring GluK2 EM and incubated at 37°C for 12 hrs. Cells were supplemented with 10mM
475 sodium butyrate and 20 μM DNQX and temperature was shifted to 30˚C at 12hrs post-infection.
476 The cell culture was incubated additional 60 hrs and harvested by low-speed centrifugation at
477 5,000 g for 20min and stored at -80˚C until use.

478 For electrophysiology experiments, human embryonic kidney 293T (HEK293T) cells were
479 cultured in Dulbecco's modified Eagle medium (DMEM, Corning) supplemented with 10% FBS at
480 37°C in a 95% O_2–5% CO_2 atmosphere. Wild-type rat GluK2 and rat GluK2 K676C/N802C DNAs
481 were cloned into the pCAG-IRES-EGFP vector (Addgene plasmid #119739). HEK293T cells were
482 transfected with 1 μg/μl cDNA using the TransIT2020 transfection reagent (Mirus) according to
483 the manufacturer's instructions. Cells expressing GluK2 wild-type were transfected for 24 hours,
484 while those expressing K676C/N802C were transfected for 18 hours. After transfection, cells were
485 dissociated using Accutase (Innovative Cell Technologies, Inc.), resuspended, and plated onto
486 35 mm poly-D-lysine-coated dishes (Neuvitro). Electrophysiological recordings were performed
487 2–4 hours later[81].

488

489 **Electrophysiological recordings**

490 All whole-cell recordings were performed using HEKA EPC10 amplifiers (HEKA Elektronik,
491 Lambrecht, Germany) with thin-wall borosilicate glass pipettes (2–5 MΩ) coated with dental wax
492 to reduce electrical noise. Currents were recorded at a holding potential of −70 mV, with a
493 sampling frequency of 10 kHz, and filtered at 2.6 kHz. The external solution contained (in mM):
494 145 NaCl, 2.5 KCl, 1.8 $CaCl_2$, 1 $MgCl_2$, 5 glucose, and 5 HEPES. The internal pipette solution
495 contained (in mM): 105 NaCl, 20 NaF, 5 Na_4BAPTA, 0.5 $CaCl_2$, 10 Na_2ATP, and 5 HEPES. The
496 pH and osmotic pressure of the external and internal solutions were adjusted to 7.4 and 300–290
497 mOsm/kg, respectively. L-glutamate was applied using theta glass tubing mounted on a
498 piezoelectric stack (MXPZT-300 series, Siskiyou) driven by a HEKA EPC10 amplifier. Typical 10–
499 90% rise times were 250–300 μs, measured from junction potentials at the open tip of the patch

500 pipette after recordings. Data acquisition was performed using PULSE software (HEKA Elektronik,
501 Lambrecht, Germany).
502
503 **Data analysis**
504 The macroscopic rate of desensitization (τ_desensitization) was measured by fitting an
505 exponential function to the decay of current from ~80% of its peak amplitude (I_peak) to baseline
506 in recordings where glutamate was applied for 1 second. For the double mutant N802C/K676C,
507 only the first exponential component, which exhibited desensitization kinetics, was considered,
508 while the steady-state current was omitted. Desensitization kinetics were fitted using a single-
509 exponential, one-term Levenberg-Marquardt fitting approach.
510 To evaluate recovery from desensitization, two protocols were employed: (1) a two-pulse
511 application of 10 mM glutamate for 100 ms per pulse, with interpulse intervals increasing in 100
512 ms steps from 50 ms to 2 s; and (2) a second protocol with interpulse intervals increasing in 2 s
513 steps, ranging from 50 ms to 20 s. In all cases, the first peak was considered the control (100%
514 activation), while the second peak represented recovery at a given time point. Data from both
515 protocols were combined, and a recovery curve was generated, plotting the percentage of
516 recovery against time. The experimental data were fitted to one-term exponential model, from
517 which the recovery time constant (τ) was derived.
518 To analyze the EC_{50} for glutamate in wild-type (WT) and mutant receptors, varying
519 concentrations of L-glutamate were applied to a single cell using a theta glass tubing mounted on
520 a piezoelectric stack (MXPZT-300 series, Siskiyou), driven by a HEKA EPC10 amplifier, for 1
521 second. One input of the theta glass tubing was connected to the control solution, while the other
522 was connected to a six-inlet manifold for different L-glutamate concentrations. A 2-minute wash
523 was used between concentration changes to ensure complete exchange before applying the next
524 solution. The L-glutamate concentrations tested were 50, 10, 1, 0.1, 0.01, and 0.001 mM, with 50
525 mM serving as the normalization reference. The normalized data are presented as mean ± S.E.M.

526 in a dose-response curve, with response on the y-axis and concentration on the x-axis.
527 Experimental data from independent biological measurements (each defined as data from one
528 cell with at least five concentration responses) were fitted to the Hill equation. The resulting EC_{50}
529 values were then averaged and presented as mean ± S.E.M.
530

531 **Non-stationary fluctuation analysis (NSFA)**

532 NSFA was performed on the decay phase of currents evoked by 200 ms applications of
533 10 mM glutamate (60–150 successive applications). Currents were sampled at 50 kHz and filtered
534 at 5 kHz. The variance and mean current were calculated for each set of currents and then binned
535 into 15 bins. The single-channel current and total number of channels (N) were determined by
536 plotting the binned variance against the binned mean current and fitting the data with a parabolic
537 function:

538 $$\sigma^2 = i\bar{I} - \frac{\bar{I}^2}{N} + \sigma_B^2$$

539 Where σ_B^2 represents the background variance, which was calculated from the baseline before
540 glutamate application. The σ_B^2 value was used to correct the variance, while the mean I_B was used
541 to correct the mean current.
542

543 **Stationary fluctuation analysis (SFA)**

544 HEK293T cells transfected with GluK2 K676C/N802C were activated with 10 mM
545 glutamate for 30 seconds, followed by a 2-minute incubation with 500 μM BPAM344. The cells
546 were then reactivated with 10 mM glutamate + 500 μM BPAM344. Currents were sampled at 10
547 kHz and filtered at 2 kHz. For each condition (glutamate alone and glutamate + BPAM344), the
548 last 10 seconds of the steady-state current were used to calculate the variance and mean current.
549 Since the stationary current represented approximately 35% of the peak current, we assumed

550 that the open probability (P_0) in the steady-state current was $P_0 < 1$. The unitary current (i) was
551 then estimated using the following equation:

552 $$i = \frac{\sigma^2}{\bar{I}}$$

553 The unitary current was then used to estimate the unitary conductance (γ) as follows:

554 $$\gamma = \frac{i}{Vm - Vr}$$

555 where V_m is the holding potential (−70 mV) and the reversal potential (V_r) is 0 mV.

556

557 The number of channels (N) was estimated using the equation:

558 $$N = \frac{\bar{I}^2}{\sigma^2}$$

559 Statistical analyses were performed using OriginLab 2025. Statistical significance was calculated
560 using a two-sided two-sample t-test, with significance assumed if $P < 0.05$.

561

562 **Protein expression and purification**

563 Cell pellets were resuspended in ice-cold lysis buffer containing 20 mM Tris-Cl (pH 8.0),
564 150 mM NaCl, 0.2 mM PMSF, 20 μg/mL DNase I, and 20 μM DNQX. Cells were lysed by
565 sonication using a Qsonica sonicator with an amplitude of 40% for 10 minutes total (10 s on, 10
566 s off). The lysate was centrifuged at 7,000 g for 20 min to remove cell debris and unbroken cells,
567 and the supernatant was subjected to ultracentrifugation at 200,000 g for 30 min to pellet the cell
568 membranes. The membrane pellet was homogenized and solubilized by gentle nutation for 2
569 hours at 4 °C in buffer consisting of 20 mM Tris-Cl (pH 8.0), 150 mM NaCl, 1% Dodecyl-β-D-
570 Maltosid (w/v, DDM), and 20 μM DNQX, followed by centrifugation at 200,000 g for 30 min to
571 remove insoluble material. The supernatant was incubated with Rho 1D4 affinity resin overnight
572 at 4 °C. The protein-bound resin was extensively washed with 100 mL of buffer consisting of 20
573 mM Tris-Cl (pH 8.0), 500 mM NaCl, 1 mM DNQX, and 0.02% DDM at room temperature, and

574 then slowly washed with 200 mL of buffer consisting of 20 mM Tris-Cl (pH 8.0), 300 mM NaCl,
575 and 0.02% DDM at room temperature at a rate of approximately 0.3 ml/min. The protein was
576 eluted in 50 mL of buffer with 20 mM Tris-Cl (pH 8.0), 300 mM NaCl, 0.02% DDM, and 0.25 mM
577 1D4 peptide. The eluted protein was concentrated and injected into a Superose 6 10/300 GL size-
578 exclusion column equilibrated with buffer containing 20 mM Tris-Cl (pH 8.0), 150 mM NaCl, and
579 0.02% DDM. The peak fractions corresponding to tetrameric GluK2 were pooled and
580 concentrated to 3.4 mg/mL for grid freezing.

581

582 **Grid preparation and cryo-EM data**

583 The cryo-EM grids were prepared as follows. UltrAuFoil R1.2/1.3 300 mesh gold grids
584 were glow-discharged for 50 seconds before sample application. A final concentration of 1 mM
585 glutamate was added to the sample, and then a droplet of 3 μL of protein sample was rapidly
586 applied onto the grids. For the BPAM344/glutamate sample, proteins were pre-incubated with 500
587 μM BPAM344 for 30 minutes on ice, followed by the addition of 1 mM glutamate to the sample.
588 3.5 μl of the protein sample was applied to the grids, and the grids are frozen within 10 seconds.
589 An FEI Vitrobot Mark IV (Thermo Fisher Scientific) was used to plunge-freeze the grids into liquid
590 ethane after sample application at 4°C and 100% humidity, with a blot time of 3 seconds and a
591 blot force of −5.

592 All cryo-EM data were collected on a Titan Krios 300 kV microscope (Thermo Fisher
593 Scientific) equipped with a GIF-Quantum energy filter (Gatan) with the slit set to 20 eV and a
594 Gatan K3 Summit direct electron detection camera (Gatan) at Case Western Reserve University.
595 Raw movies were collected using EPU in super-resolution mode, with a physical image pixel size
596 of 1.06 Å and a defocus range of −0.8 to −1.6 μm. The total dose of around 50 e^{-}/Å² was used
597 for each movie, distributed across 50 frames for a total exposure time of approximately 3.2
598 seconds.

599

600 **Cryo-EM image processing**

601 For dataset **a** (GluK2 K676C/N802C supplemented with 1 mM glutamate and 500 μM
602 BPAM344), the same motion correction procedure was applied using Patch Motion Correction in
603 CryoSPARC4. CTF calculations were also carried out on the motion-corrected images using
604 Patch CTF Estimation in CryoSPARC4. Micrographs unsuitable for further analysis were manually
605 removed. Initial particle selection from 1000 micrographs was done with Blob Picker, followed by
606 2D classification to generate good templates. Template Picker was used to pick 903,654 particles,
607 which were extracted with a pixel size of 2.12 Å. After several rounds of 2D classification, 612,540
608 particles were selected for initial 3D model generation via ab initio reconstruction. A total of
609 352,269 particles were selected and re-extracted with a pixel size of 1.06 Å following multiple
610 rounds of heterogeneous refinement. NU-refinement for each class resulted in maps with
611 resolutions of 6.16 Å, 5.80 Å, 4.14 Å, 4.00 Å, 4.00 Å, and 3.83 Å, respectively.

612 For dataset **b** (GluK2 K676C/N802C supplemented with 1 mM glutamate), the raw movie
613 stacks were motion-corrected using Patch Motion Correction in CryoSPARC4. The Contrast
614 Transfer Function (CTF) was calculated from the motion-corrected images using the Patch CTF
615 Estimation in CryoSPARC4. Micrographs deemed unsuitable for further analysis were removed
616 through manual inspection. Initial particle selection was performed using Blob Picker from 2,000
617 micrographs, followed by 2D classification to generate good templates. Subsequently, 1,005,623
618 particles were picked using Template Picker and extracted with a pixel size of 2.12 Å. After several
619 rounds of 2D classification, 765,893 particles were selected to generate the initial 3D model
620 through ab initio reconstruction. A total of 277,369 particles were selected and re-extracted with
621 a pixel size of 1.06 Å after multiple rounds of heterogeneous refinement. NU-refinement for each
622 class yielded maps with resolutions of 3.92 Å, 4.35 Å, 3.85 Å, and 3.82 Å, respectively.

623 To improve the structure resolution for classes present in both datasets, particles from each class
624 were combined and subjected to several rounds of heterogeneous refinement to remove junk

625 particles. Separate NU-refinements for each class generated maps with resolutions of 3.67 Å,
626 4.02 Å, 3.81 Å, and 3.74 Å, respectively. For Class 2, focused masks around the ATD and LBD-
627 TMD regions were created separately and used for local refinements of the corresponding regions.
628 As a result, 3.42 Å reconstruction of the ATD region and 3.86 Å reconstruction of the LBD-TMD
629 region were obtained through local refinement with focused masks. For the non-desensitized state,
630 particle subtraction was performed for both ATD-focused and LBD-TMD-focused heterogeneous
631 refinement. After several rounds of heterogeneous refinement, 80,325 particles were used for
632 subsequent NU-refinement, resulting in a 3.70 Å resolution of the ATD 3D reconstruction. A total
633 of 117,714 particles were subjected to NU-refinement for the LBD-TMD region, generating 3.93
634 Å maps. The Gold-standard Fourier Shell Correlation (FSC) 0.143 criteria were used to estimate
635 the map resolution for each class. For the shallow-desensitized state, focused masks around the
636 ATD and LBD-TMD regions were created separately and used for local refinements of the
637 corresponding regions. As a result, 3.42 Å reconstruction of the ATD region and 3.86 Å
638 reconstruction of the LBD-TMD region were obtained through local refinement with focused
639 masks.
640
641 **Model building and refinement**
642 The model building for the non-desensitized class was initiated by individually fitting rigid-
643 body components of the LBD extracted from the BPAM344-, and ConA-bound GluK2 structure
644 (PDB code 9B36), and the TMD and ATD from the BPAM344 bound GluK2 structure (PDB code
645 8FWQ) into the cryo-EM map using Chimera. Subsequent manual adjustments, including fitting
646 the backbone and side chains of the ATD-LBD and LBD-TM3 linkers into the density, as well as
647 deleting unresolved side chains and making subtle local adjustments to minimize clashes, were
648 performed in Coot.
649 For the shallow-desensitized class, the single LBD, entire ATD, and TMD were separately
650 extracted from the BPAM344 bound GluK2 structure (PDB code 8FWQ) and manually docked

651 into the corresponding cryo-EM map using Chimera. Further manual adjustments of the backbone
652 and side chains were completed in Coot.

653 For intermediate and deep-desensitized classes, the single LBD, entire ATD, and TMD
654 were extracted from the deep-desensitized GluK2 structure (PDB: 5KUF) and individually docked
655 into the corresponding cryo-EM maps for each class using Chimera. Additional manual
656 adjustments to the backbone and side chains were completed in Coot.

657 All four initial models were then refined in real space using Phenix against the
658 corresponding cryo-EM maps. The models were validated through comprehensive validation
659 procedures in Phenix. Glutamate ligands and BPAM344 compounds were extracted from the
660 cryo-EM structure (PDB code 9B36) and manually fitted into the corresponding densities in Coot.

661

662 **Key source table**

Reagent type (species) or resource	**Designation**	**Source or reference**	**Identifiers**	**Additional information**
Gene (*Rattus norvegicus*)	GRIK2_RAT	Genscript (synthesized)	P42260	
Cell line (*Homo sapiens*)	HEK293S GnTI-	ATCC	Cat. No. CRL-3022	
Cell line (*Homo sapiens*)	HEK293T	ATCC	Cat. No. CRL-3216	
Cell line (insect)	Sf9	Novagen	Cat. No. 71104	

Chemical compound, drug	L-glutamate	Sigma Aldrich	Cat. No. 49621	
Software, algorithm	Pulse	HEKA	https://scicrunch.org/resolver/SCR_018399	https://www.heka.com/
Software, algorithm	OriginPro 2020	OriginLab	RRID:SCR_014212	https://www.originlab.com/2020
Software, algorithm	cryoSPARC 4.	doi:10.1038/nmeth.4169.	RRID:SCR_016501	https://cryosparc.com/
Software, algorithm	UCSF Chimera	doi:10.1002/jcc.20084	RRID:SCR_004097	http://plato.cgl.ucsf.edu/chimera/
Software, algorithm	UCSF ChimeraX	doi:10.1002/pro.3943	RRID:SCR_015872	https://www.cgl.ucsf.edu/chimerax/
Software, algorithm	HOLE	doi:10.1016/s0263-7855(97)00009-x		http://www.holeprogram.org
Software, algorithm	COOT 0.9x	doi:10.1107/S0907444910007493	RRID:SCR_014222	http://www2.mrc-lmb.cam.ac.uk/personal/pemsley/coot/
Software, algorithm	Phenix 1.20	doi:10.1107/S2059798319011471	RRID:SCR_014224	https://www.phenix-online.org/

Software, algorithm	MolProbity	doi:10.1107/S0907444909042073	RRID:SCR_014226	http://molprobity.biochem.duke.edu
Software, algorithm	deepEMhancer	https://doi.org/10.1038/s42003-021-02399-1		https://github.com/rsanchezgarc/deepEMhancer

663

664 **Acknowledgment**

665 We thank Dr. Matthias Buck (CWRU) for discussion and critical feedback on the manuscript. We
666 thank Drs. Kunpeng Li and Kyle Whiddon at Case Western Reserve University (CWRU) for their
667 cryo-EM technical support, and the High-Performance Computing Resource CWRU Core facility
668 for their computational support. We are grateful to Drs. Corey Smith and Shyue-An Chan at
669 CWRU for their technical assistance with patch-clamp electrophysiology. We thank Ashlee
670 Hoffman (CWRU) for proofreading the manuscript. This work was funded by the National Institute
671 of Health (1R35GM147266-01 to N.T.), Whitehall Foundation (N.T.), and American Heart
672 Association https://doi.org/10.58275/AHA.23POST1019193.pc.gr.174253 (S.G.).

673

674 **Author contributions**

675 C.Z., S.G., and N.T. conceived the project and designed the experimental procedures. C.Z.
676 designed the constructs, conduced the protein expression and purification, and performed the EM
677 data collection and data analysis. S.G. conducted electrophysiological recordings. C.Z., S.G., and
678 N.T. wrote the manuscript. All authors reviewed the final draft.

679

680 **Competing interests**

681 The authors declare no competing interests.

682

683 **Data and materials availability**

684 Cryo-EM density maps and atomic coordinates for GluK2-apo and GluK2-domoate were
685 deposited in the electron microscopy data bank under the accession codes listed below.

686

Name	Accession code
GluK2 ATD in the non-desensitized state	PDB 9MZQ, EMD-48765
GluK2 LBD-TMD bound to BPAM344 and glutamate in the non-desensitized state	PDB 9MZR, EMD-48766
GluK2 bound to BPAM344 and glutamate in the non-desensitized state, composite map	PDB 9MZS, EMD-48767
GluK2 ATD in the shallow-desensitized state	PDB 9MZN, EMD-48762
GluK2 LBD-TMD in the shallow-desensitized state	PDB 9MZO, EMD-48763
GluK2 in the shallow-desensitized state, consensus map	PDB 9MZM, EMD-48761
GluK2 in the shallow-desensitized state, composite map	PDB 9MZP, EMD-48764
GluK2 in the intermediate state	PDB 9MZL, EMD-48760
GluK2 in the deep-desensitized state 1	PDB 9MZK, EMD-48759
GluK2 in the deep-desensitized state 2	PDB 9MZJ, EMD-48758
GluK2 in the deep-desensitized state 3	PDB 9MZI, EMD-48757

687

688

689 **Figure legends**

690 **Figure 1. Functional and structural characterization of GluK2 K676C/N802C.**

691 **(A)** Representative whole-cell patch-clamp trace showing response of GluK2 WT or GluK2
692 K676C/N802C to a 20-second application of 1 mM glutamate in the absence and presence of
693 BPAM344 (BPAM). Arrows indicate the maximum peak current (I_{peak}) and the steady-state current

694 (I_{ss}). **(B)** Quantification of percent desensitization for currents evoked by 1 mM glutamate. **(C)**
695 Potentiation of the peak current amplitudes (I_{peak}) of GluK2 WT (left), the peak current amplitudes
696 (I_{peak}) of K676C/N802C (middle), and the steady-state current amplitude (I_{ss}) of GluK2
697 K676C/N802C measured in the presence of BPAM344 compared to currents in the absence of
698 BPAM344. **(D)** Cryo-EM map and model of GluK2 K676C/N802C in complex with glutamate and
699 BPAM344 in a non-desensitized/non-active state. **(E)** Chemical structure of BPAM344. **(F)**
700 Structure of the LBD layer viewed parallel to the membrane, with BPAM344 and glutamate shown
701 as space-filling models, colored pink and cyan, respectively. **(G)** Close-up view of the BPAM344
702 binding site at the AD subunit interface, indicating by a black dotted box in panel F. **(H)**
703 Comparison of the apo GluK2 LBD (PDB code 9CAZ) and the glutamate-bound GluK2 LBD in the
704 non-desensitized LBD conformation. The LBD is a bi-lobed structure, consisting of D1 and D2
705 lobes, with glutamate binding in the cleft between them. The D1 lobe is superimposed, and the
706 rotation angles to align the D2 residues were calculated. The glutamate-bound bi-lobe is closed
707 20° than the apo state LBD conformation. **(I)** Cryo-EM density for bound glutamate and the
708 surrounding residues in the agonist binding pocket. **(J)** The cryo-EM densities for disulfide bonds
709 between K676C and N802C in AB and CD subunits. The crosslinks in the LBD layers are indicated
710 by the red dotted box in the panel F.

711

712 **Figure 2. Structural mechanism of GluK2 upon activation and desensitization.**

713 **(A)** Comparison of Cryo-EM reconstructions and models of BPAM344- and glutamate-bound
714 GluK2 K676C/N802C in a non-desensitized conformation, and BPAM344-, glutamate-, and
715 Concanavalin A-bound GluK2 in an open (active) state (PDB code 9B36). The distances between
716 S700 in the AC subunits and E788 in the BD subunits at the LBD dimer-dimer interface are colored
717 red and blue, respectively. **(B)** Structural comparison of LBD dimers in the non-desensitized and
718 open GluK2, viewed perpendicular to the membrane. The locations of the centers of mass (COM)

719 of D1 and D2 are indicated by blue and green spheres, respectively, with the COM distances
720 between D1 and D2 of subunit AD LBDs (shown as circles) displayed below. Arrows indicate LBD
721 bi-lobe closure, with the D2 lobe moving closer to D1. Distances between the Cα atoms of P773
722 (D1-D1 distance) and S670 (D2-D2 distance) in the AD subunits are also indicated. **(C)**
723 Comparison of LBD-TM3 linkers and TM3 formation in BPAM344-bound, agonist-unbound GluK2
724 (PDB code 8FWS)[32] and non-desensitized GluK2, showing the subunit BD pair (left) and the
725 subunit AC pair (right). S670 is shown as spheres in corresponding colors for the non-
726 desensitized state and in gray for BPAM344-bound GluK2. The cross-dimer distances between
727 the Cα atoms of S670 (in the BD and AC subunit pairs) are indicated above. Residues forming
728 the ion channel pore are displayed as sticks. The locations of the TM3 gating hinge at A656
729 (subunit BD) and E662 (subunit AC) in the non-desensitized conformation are highlighted in red.
730 The dotted line indicates the positions of pore-lining residues: (1) M664, (2) T660, (3) A656, and
731 (4) T652. (2') E662, which serves as the gating hinge, is also highlighted in this panel. Helices
732 surrounding T664 and M664 in subunit BD, as well as helices around M664 in subunit AC, are
733 unwound in the non-desensitized conformation. As a result, the ion channel pore above the gating
734 region in the non-desensitized conformation is wider compared to that in the BPAM344-bound
735 GluK2 structure, with black allows indicating the conformational changes. **(D)** Comparison of LBD-
736 TM3 linkers and TM3 formation in non-desensitized GluK2 and BPAM344-, ConA- and glutamate
737 bound open GluK2 (PDB code 9B36)[27], showing the subunit BD pair (left) and subunit AC pair
738 (right). The cross-dimer distances between the Cα atoms of S670 are indicated above. Residues
739 forming the ion channel pore are displayed as sticks. The locations of the gating hinge at L655 in
740 A-D subunits of the open GluK2 (PDB 9B36) structure are highlighted in gray, for comparison with
741 the gating hinge in the non-desensitized conformation shown in panel C. The dotted line indicates
742 the positions of pore-lining residues: (1) M664, (2) T660, (3) A656, and (4) T652, as well as (4')
743 L655, which forms the gating hinge. Yellow, green, blue, and pink arrows indicate the
744 rearrangement of TM3 in each subunit during the transition from the non-desensitized to the open

745 conformation. **(E)** Pore profile in the non-desensitized and open (PBD 9B36) structures. Pore-
746 delineating dots are colored according to pore radius: red for regions with a radius less than 1.1
747 Å and gray for regions with a radius greater than 1.1 Å, which would allow passage of a
748 dehydrated ion (1.1 Å for calcium). **(F)** The pore radius for the non-desensitized (red) and open
749 (PDB 9B36, gray) conformations, calculated using HOLE.

750

751 **Figure 3. Structures of GluK2 in desensitized states.**

752 **(A)** Three-dimensional (3D) cryo-EM reconstructions of glutamate-bound GluK2 K676C/N802C
753 in desensitized conformations. **(B)** Top views of glutamate-bound GluK2 K676C/N802C, focusing
754 on the LBD layers. The in-plane rotation angles of the LBDs are indicated. Disulfide bonds formed
755 between the two LBD dimers are highlighted in red dotted boxes. **(C)** Close-up view of the disulfide
756 bonds between K676C and N802C at the CD subunit interface (left) and the AC subunit interface
757 (right) in the shallow-desensitized conformation. **(D)** Top view of the LBD layer in the deep-
758 desensitized conformation, highlighting helices E and G, which form the desensitization ring. The
759 view is parallel to the membrane, with coloring consistent with panel A. **(E)** The desensitization
760 ring formed in three deep-desensitized conformations, viewed perpendicular to the membrane.
761 The in-plane rotation of the LBD shown in panel B shifts the LBD-TM3 linker, positioning it above
762 the ion channel pore formed by the TM3 helices.

763

764 **Figure 4. GluK2 stabilized in a shallow-desensitized-like conformations resembbles the**
765 **desensitized conformation of AMPARs.**

766 **(A, B)** Structural comparison between the non-desensitized and shallow-desensitized
767 conformations, viewed parallel (A) and perpendicular (B) to the membrane. Black arrows indicate
768 the degree of LBD domain rotation. **(C, D)** Structural comparison of LBD layers in GluK2
769 K676C/N802C in the shallow-desensitized state and GluA2 AMPAR in the desensitized state

770 (PDB code 7RYZ)[64], viewed parallel (C) and perpendicular (D) to the membrane. Distances
771 between S700 in the AC subunits and E788 in the BD subunits at the LBD dimer-dimer interface
772 are shown in red and blue, respectively. The locations of the centers of mass (COM) of D1 and
773 D2 are indicated by blue and green spheres, respectively, with the COM distances between D1
774 and D2 of subunit AD LBDs (shown as circles) displayed below. Arrows indicate D1 lobe rotations
775 compared to the non-desensitized (KAR) or apo (AMPAR) states. Distances between the Cα
776 atoms of P773 (D1-D1 distance) and S670 (D2-D2 distance) in the AD subunits are also indicated.
777 **(E)** Comparison of LBD-TM3 linkers and TM3 helices in non-desensitized and shallow-
778 desensitized conformations, showing the subunit BD pair (left) and subunit AC pair (right). S670
779 is shown as spheres in corresponding colors for the shallow-desensitized conformation and in
780 gray for the non-desensitized conformation. The cross-dimer distances between the Cα atoms of
781 S670 are indicated. Residues forming the ion channel pore are displayed as sticks. The locations
782 of the TM3 gating hinge at T660 (subunit BD) and M664 (subunit AC) in the shallow-desensitized
783 conformation are highlighted in red. The dotted line indicates the positions of pore-lining residues:
784 (1) M664, (2) T660, (3) A656, and (4) T652. The shallow-desensitized conformation contains an
785 additional half-turn of helices at T660 compared to the non-desensitized conformation. **(F)**
786 Comparison of LBD-TM3 linkers and TM3 formation in shallow- and deep-desensitized GluK2,
787 showing the subunit BD pair (left) and the subunit AC pair (right). S670 is represented as spheres
788 in corresponding colors for the deep-desensitized state and in gray for the shallow-desensitized
789 GluK2. In the deep-desensitized conformation, the ion channel is sealed at M664, completely
790 closing the ion channel pore, in contrast to the shallow-desensitized conformation, which has a
791 kink at T660 in the BD subunits.

792

793 **Figure 5. Ion channel pore of desensitized GluK2 KAR.**

794 **(A)** Permeation pathway dictating pore diameter of GluK2 K676C/N802C in desensitized states.
795 Pore-delineating dots are colored according to pore radius: red for regions with a radius less than
796 1.1 Å and gray for regions with a radius greater than 1.1 Å. **(B)** Permeation pathway determining
797 the pore diameter of the GluA2 AMPAR in a desensitized state (PDB code 7RYZ)[64], using the
798 same color code as (A). **(C–D)** Pore profile traces comparing GluK2 K676C/N802C KAR.
799 Comparison between the shallow-desensitized conformation and the desensitized GluA2 AMPAR
800 (PDB: 7RYZ) (C); and comparison among three deep-desensitized states (D).

801

802 **Figure 6. Functional characterization of GluK2 K676C/N802C receptor.**

803 **(A)** Representative whole-cell patch-clamp recordings of GluK2 WT (left) and GluK2
804 K676C/N802C (right) in response to varying concentrations of glutamate (0.001–50 mM). The
805 black bar at the top of the recording represents the glutamate application. The cells were held at
806 -70 mV. **(B)** Quantification of current density (pA/pF) at the peak current for GluK2 WT (gray) and
807 K676C/N802C mutant (blue) activated by 10 mM glutamate. No significant differences were
808 observed (NS, $p > 0.05$). **(C)** Glutamate dose-response curves for GluK2 WT (n=12) and
809 K676C/N802C (n=8), normalized to the maximal response at 50 mM glutamate. Glutamate was
810 applied for 1 s, and the peak current was measured at each concentration. All response were
811 recorded at each concentrations using a single cell. **(D)** EC_{50} values for glutamate activation of
812 GluK2 WT (gray) and K676C/N802C (blue). No significant differences were detected (NS, $p >$
813 0.05). **(E)** Ratio of steady-state to peak current ($I_{steady\text{-}state}$ / I_{peak}) at various glutamate
814 concentrations. The values of the steady-state current were taken at the end of the activation. **(F)**
815 Representative current traces of GluK2 WT (black) and GluK2 K676C/N802C (blue) during a two-
816 pulse protocol, showing the interval between glutamate exposures ranging from 50 ms to 20 s,
817 highlighting altered desensitization kinetics in the mutant. **(G)** Recovery from desensitization at
818 increasing inter-sweep intervals, fitted with one-term exponential functions for GluK2 WT

819 (R^2=0.99) and two-term exponential functions for GluK2 K676C/N802C (R^2=0.99). GluK2
820 K676C/N802C exhibits a faster recovery than GluK2 WT. **(H)** Time constant (τ) of recovery from
821 desensitization, showing a significant reduction in τ for the K676C/N802C mutant ($p < 0.0001$,
822 two-sided two-sample t-test). The data for the WT was obtained from the fit in panel G, and for
823 K676C/N802C, a mean τ was calculated using $\tau_{mean} = ((A1\ \tau1 + A2\ \tau2) / (A1 + A2))$. Biological
824 independent measurements: n=9 for GluK2 WT and n=9 for GluK2 K676C/N802C.

825 Error bars represent Standard Deviation (SD). Statistical significance is indicated as NS (not
826 significant) or with p-values where appropriate.

827

828 **Figure 7. Cysteine crosslinking modulates the kinetics of GluK2 K676C/N802C**

829 **(A)** Representative whole-cell patch-clamp recordings of GluK2 WT (left) and GluK2
830 K676C/N802C (right) in the presence of 10 mM glutamate before (black) and after treatment with
831 5 mM DTT for 7 minutes (red). **(B)** Quantification of the I_{ss}/I_{peak} ratio in GluK2 K676C/N802C before
832 (blue) and after (red) DTT treatment, showing a significant reduction in steady-state current post-
833 treatment ($p < 0.0001$, two-sided two-sample t-test). **(C)** Recovery from desensitization at
834 increasing inter-sweep intervals after treatment with 5 mM DTT. The GluK2 WT recovery curve
835 from Figure 6, panel C is shown in black for comparison. The recovery kinetics of GluK2
836 K676C/N802C post-DTT treatment were fitted with a one-term exponential function ($R^2 = 0.98$),
837 showing a recovery profile similar to WT. **(D)** Time constant (τ) of recovery from desensitization,
838 showing that DTT treatment restores the recovery kinetics of GluK2 K676C/N802C to a level
839 comparable to WT (NS, $p > 0.05$). **(E)** Representative whole-cell responses to 10 mM glutamate
840 (200 ms, -70 mV; black bar) from HEK293T cells expressing GluK2 WT (left, average current in
841 black, 60 individual responses in gray) and GluK2 K676C/N802C (right, average current in blue,
842 100 individual responses in gray). Inset: Current-variance relationship, with WT data fitting a
843 parabolic function (dotted line), whereas the K676C/N802C mutant does not follow this trend. **(F)**

844 Whole-cell recordings of GluK2 K676C/N802C in response to 10 mM glutamate in the absence
845 (blue) and presence (green) of 500 μM BPAM344. Right panel: Representative noise traces at
846 the end of glutamate application (~10 s) under both conditions, indicated by blue and green boxes.
847 Background noise (baseline) was taken from the current recording before glutamate application,
848 as indicated by the gray box. **(G)** Variance-mean current relationship for individual cells in the
849 presence of glutamate alone or with BPAM344, indicating an enhanced channel variance-current
850 relationship upon BPAM344 application. **(H)** Unitary conductance determined by variance-mean
851 analysis, showing no significant difference between two conditions with and without BPAM344
852 (NS, $p > 0.05$). (I) Estimated number of open channels, showing a significant increase upon
853 BPAM344 application ($p = 0.0025$, two-sided paired t-test). Biologically independent
854 measurements: $n = 6$. Data for glutamate and BPAM344 conditions were obtained from the same
855 cell.

856 Error bars represent standard deviation (SD). Statistical significance is indicated as NS (not
857 significant) or with p-values where appropriate.

858

859 **Figure 8. Schematic representation of conformational rearrangements during activation**
860 **and desensitization.** The proposed model illustrates how conformational changes in the LBD
861 layers during desensitization regulate ion channel permeation. Wild-type GluK2 typically
862 transitions into a deeply desensitized state, adopting a stabilized, classically four-fold symmetrical
863 conformation. By contrast, receptors that stabilize in a two-fold symmetrical, desensitized
864 AMPAR-like conformation, maintained by engineered disulfide bonds, remain conductive,
865 although their conductivity is lower than that of receptors in the open state. The position of the
866 gating kink differs among the non-desensitized, open, and shallow-desensitized conformations.
867 Additionally, the ATD layers elevate and rotate in both the non-desensitized (non-active) and
868 open-state GluK2 conformations.

869

870 **Figure S1. Design of the double cysteine crosslink mutant of GluK2.**

871 **(A)** Schematic illustration of the KAR subunit topology. Each KAR subunit is composed of four
872 domains: ATD, LBD,TMD, and CTD. The LBD contains two segments termed D1 (upper lobe)
873 and D2 (lower lobe). Agonists bind to the interface between the D1 and D2 lobes of the LBD. **(B)**
874 Homology model of the active GluK2 KAR, generated based on the active GluA2 AMPAR (PDB
875 code 5WEO) as a template. **(C)** The inter-protomer interface between subunit A and subunit B in
876 the homology model. **(D)** The distance between residues K676 and N802 in the BPAM344-,
877 concanavalin A-, and glutamate-bound open/active GluK2 (PDB code 9B36)[27], BPAM344-bound
878 (without orthosteric ligands) inactive GluK2 (PDB code 8FWS)[32], and glutamate-bound deep
879 desensitized GluK2 (PDB code 9B38)[27] structures. **(E, F)** Two designed disulfide crosslinks at the
880 inter-protomer interface, shown in the homology model and the schematic figure.

881

882 **Figure S2. Channel properties of the single cysteine mutant and protein preparation.**

883 **(A)** Representative electrophysiological traces from HEK293T cells expressing GluK2 WT, GluK2
884 K676C, and GluK2 N802C, activated by 10 mM glutamate. **(B)** Size exclusion chromatography
885 profile of the GluK2 N802C/K676C mutant eluted from the Superose 6 column chromatography.
886 The fractions used for the cryo-EM studies are indicated by the black dotted line. **(C)** SDS-PAGE
887 analysis of the purified GluK2 N802C/K676C mutant, with the black line indicating the full-length
888 GluK2 protein band.

889

890 **Figure S3. Cryo-EM data processing workflow for structures of the GluK2 K676C/N802C**
891 **mutant in the presence of glutamate and BPAM344 (a), and glutamate alone (b)**

892

Figure S4. Cryo-EM analysis of GluK2 K676C/N802C.

(A, D) Local resolution maps, **(B, E)** Fourier shell correlation (FSC) curves. The threshold was set at 0.143 for unmasked and masked curves, and a 0.5 threshold was used for the map-to-model curve. **(C, F)** Angular distribution of particles calculated using the 3D refinement reconstruction algorithm in cryoSPARC.

Figure S5. Comparison of ATD-LBD layers.

(A) GluK2 structures, aligned parallel to the membrane. The distances between the center-of-mass (COM, black circles) of the ATD and LBD layers are indicated. **(B)** Superimposition of the ATD layer in the non-desensitized, intermediate, and desensitized GluK2 structures. The color codes match those in panel A. **(C)** ATD-LBD rotation. The LBD layers in the BPAM344- and glutamate-bound non-desensitized, and the BPAM344-, ConA-, and glutamate-bound open GluK2 conformations, are rotated counterclockwise when the ATD layers are superimposed.

Figure S6. Models and cryo-EM densities of the transmembrane domain.

TM3 helices in non-desensitized, shallow-desensitized, intermediate, and deep-desensitized structures, with the protein structural model shown as ribbons and sticks. Cryo-EM densities are displayed in transparent gray.

References

1 Hansen, K. B. *et al.* Structure, Function, and Pharmacology of Glutamate Receptor Ion Channels. *Pharmacol Rev* **73**, 298-487 (2021). https://doi.org:10.1124/pharmrev.120.000131

2 Lerma, J. Roles and rules of kainate receptors in synaptic transmission. *Nat Rev Neurosci* **4**, 481-495 (2003). https://doi.org:10.1038/nrn1118

3 Chittajallu, R. *et al.* Regulation of glutamate release by presynaptic kainate receptors in the hippocampus. *Nature* **379**, 78-81 (1996). https://doi.org:10.1038/379078a0

4 Rodríguez-Moreno, A., Herreras, O. & Lerma, J. Kainate receptors presynaptically downregulate GABAergic inhibition in the rat hippocampus. *Neuron* **19**, 893-901 (1997). https://doi.org:10.1016/s0896-6273(00)80970-8

5 Cossart, R. *et al.* Presynaptic kainate receptors that enhance the release of GABA on CA1 hippocampal interneurons. *Neuron* **29**, 497-508 (2001). https://doi.org:10.1016/s0896-6273(01)00221-5

6 Polenghi, A. *et al.* Kainate Receptor Activation Shapes Short-Term Synaptic Plasticity by Controlling Receptor Lateral Mobility at Glutamatergic Synapses. *Cell Rep* **31**, 107735 (2020). https://doi.org:10.1016/j.celrep.2020.107735

7 Ramos, C. *et al.* Activation of Extrasynaptic Kainate Receptors Drives Hilar Mossy Cell Activity. *J Neurosci* **42**, 2872-2884 (2022). https://doi.org:10.1523/jneurosci.0922-21.2022

8 Lerma, J. & Marques, J. M. Kainate receptors in health and disease. *Neuron* **80**, 292-311 (2013). https://doi.org:10.1016/j.neuron.2013.09.045

9 Aller, M. I., Pecoraro, V., Paternain, A. V., Canals, S. & Lerma, J. Increased Dosage of High-Affinity Kainate Receptor Gene grik4 Alters Synaptic Transmission and Reproduces Autism Spectrum Disorders Features. *J Neurosci* **35**, 13619-13628 (2015). https://doi.org:10.1523/jneurosci.2217-15.2015

10 Begni, S. *et al.* Association between the ionotropic glutamate receptor kainate 3 (GRIK3) ser310ala polymorphism and schizophrenia. *Mol Psychiatry* **7**, 416-418 (2002). https://doi.org:10.1038/sj.mp.4000987

11 Shaltiel, G. *et al.* Evidence for the involvement of the kainate receptor subunit GluR6 (GRIK2) in mediating behavioral displays related to behavioral symptoms of mania. *Mol Psychiatry* **13**, 858-872 (2008). https://doi.org:10.1038/mp.2008.20

12 Shibata, H. *et al.* Association study of polymorphisms in the GluR7, KA1 and KA2 kainate receptor genes (GRIK3, GRIK4, GRIK5) with schizophrenia. *Psychiatry Res* **141**, 39-51 (2006). https://doi.org:10.1016/j.psychres.2005.07.015

13 Diguet, E. *et al.* Experimental basis for the putative role of GluR6/kainate glutamate receptor subunit in Huntington's disease natural history. *Neurobiol Dis* **15**, 667-675 (2004). https://doi.org:10.1016/j.nbd.2003.12.010

953 14 Schiffer, H. H. & Heinemann, S. F. Association of the human kainate receptor GluR7 gene
954 (GRIK3) with recurrent major depressive disorder. *Am J Med Genet B Neuropsychiatr*
955 *Genet* **144b**, 20-26 (2007). https://doi.org:10.1002/ajmg.b.30374

956 15 Pickard, B. S. *et al.* A common variant in the 3'UTR of the GRIK4 glutamate receptor gene
957 affects transcript abundance and protects against bipolar disorder. *Proc Natl Acad Sci U*
958 *S A* **105**, 14940-14945 (2008). https://doi.org:10.1073/pnas.0800643105

959 16 Catches, J. S., Xu, J. & Contractor, A. Genetic ablation of the GluK4 kainate receptor
960 subunit causes anxiolytic and antidepressant-like behavior in mice. *Behav Brain Res* **228**,
961 406-414 (2012). https://doi.org:10.1016/j.bbr.2011.12.026

962 17 Lowry, E. R., Kruyer, A., Norris, E. H., Cederroth, C. R. & Strickland, S. The GluK4 kainate
963 receptor subunit regulates memory, mood, and excitotoxic neurodegeneration.
964 *Neuroscience* **235**, 215-225 (2013). https://doi.org:10.1016/j.neuroscience.2013.01.029

965 18 Matute, C. Therapeutic potential of kainate receptors. *CNS Neurosci Ther* **17**, 661-669
966 (2011). https://doi.org:10.1111/j.1755-5949.2010.00204.x

967 19 Jane, D. E., Lodge, D. & Collingridge, G. L. Kainate receptors: pharmacology, function
968 and therapeutic potential. *Neuropharmacology* **56**, 90-113 (2009).
969 https://doi.org:10.1016/j.neuropharm.2008.08.023

970 20 Negrete-Díaz, J. V., Falcón-Moya, R. & Rodríguez-Moreno, A. Kainate receptors: from
971 synaptic activity to disease. *Febs j* **289**, 5074-5088 (2022).
972 https://doi.org:10.1111/febs.16081

973 21 Swanson, G. T. Targeting AMPA and kainate receptors in neurological disease: therapies
974 on the horizon? *Neuropsychopharmacology* **34**, 249-250 (2009).
975 https://doi.org:10.1038/npp.2008.158

976 22 Cui, C. & Mayer, M. L. Heteromeric kainate receptors formed by the coassembly of GluR5,
977 GluR6, and GluR7. *J Neurosci* **19**, 8281-8291 (1999).
978 https://doi.org:10.1523/jneurosci.19-19-08281.1999

979 23 Mulle, C. *et al.* Subunit composition of kainate receptors in hippocampal interneurons.
980 *Neuron* **28**, 475-484 (2000). https://doi.org:10.1016/s0896-6273(00)00126-4

981 24 Reiner, A., Arant, R. J. & Isacoff, E. Y. Assembly stoichiometry of the GluK2/GluK5 kainate
982 receptor complex. *Cell Rep* **1**, 234-240 (2012).
983 https://doi.org:10.1016/j.celrep.2012.01.003

984 25 Selvakumar, P. *et al.* Structural and compositional diversity in the kainate receptor family.
985 *Cell Rep* **37**, 109891 (2021). https://doi.org:10.1016/j.celrep.2021.109891

986 26 Mayer, M. L. Structural biology of kainate receptors. *Neuropharmacology* **190**, 108511
987 (2021). https://doi.org:10.1016/j.neuropharm.2021.108511

988 27 Gangwar, S. P. *et al.* Kainate receptor channel opening and gating mechanism. *Nature*
989 (2024). https://doi.org:10.1038/s41586-024-07475-0

990 28 Meyerson, J. R. *et al.* Structural basis of kainate subtype glutamate receptor
991 desensitization. *Nature* **537**, 567-571 (2016). https://doi.org:10.1038/nature19352

992 29 Khanra, N., Brown, P. M., Perozzo, A. M., Bowie, D. & Meyerson, J. R. Architecture and
993 structural dynamics of the heteromeric GluK2/K5 kainate receptor. *Elife* **10** (2021).
994 https://doi.org:10.7554/eLife.66097

995 30 He, L. *et al.* Kainate receptor modulation by NETO2. *Nature* (2021).
996 https://doi.org:10.1038/s41586-021-03936-y

997 31 Kumari, J., Vinnakota, R. & Kumar, J. Structural and Functional Insights into GluK3-
998 kainate Receptor Desensitization and Recovery. *Sci Rep* **9**, 10254 (2019).
999 https://doi.org:10.1038/s41598-019-46770-z

1000 32 Gangwar, S. P., Yen, L. Y., Yelshanskaya, M. V. & Sobolevsky, A. I. Positive and negative
1001 allosteric modulation of GluK2 kainate receptors by BPAM344 and antiepileptic
1002 perampanel. *Cell Rep* **42**, 112124 (2023). https://doi.org:10.1016/j.celrep.2023.112124

1003 33 Kumari, J. *et al.* Structural dynamics of the GluK3-kainate receptor neurotransmitter
1004 binding domains revealed by cryo-EM. *Int J Biol Macromol* **149**, 1051-1058 (2020).
1005 https://doi.org:10.1016/j.ijbiomac.2020.01.282

1006 34 Gangwar, S. P. *et al.* Trapping of spermine, Kukoamine A, and polyamine toxin blockers
1007 in GluK2 kainate receptor channels. *Nat Commun* **15**, 10257 (2024).
1008 https://doi.org:10.1038/s41467-024-54538-x

1009 35 Paternain, A. V., Rodríguez-Moreno, A., Villarroel, A. & Lerma, J. Activation and
1010 desensitization properties of native and recombinant kainate receptors.
1011 *Neuropharmacology* **37**, 1249-1259 (1998). https://doi.org:10.1016/s0028-
1012 3908(98)00098-7

1013 36 Weston, M. C., Schuck, P., Ghosal, A., Rosenmund, C. & Mayer, M. L. Conformational
1014 restriction blocks glutamate receptor desensitization. *Nat Struct Mol Biol* **13**, 1120-1127
1015 (2006). https://doi.org:10.1038/nsmb1178

1016 37 Jones, M. V. & Westbrook, G. L. The impact of receptor desensitization on fast synaptic
1017 transmission. *Trends Neurosci* **19**, 96-101 (1996). https://doi.org:10.1016/s0166-
1018 2236(96)80037-3

1019 38 Meyerson, J. R. *et al.* Structural mechanism of glutamate receptor activation and
1020 desensitization. *Nature* **514**, 328-334 (2014). https://doi.org:10.1038/nature13603

1021 39 Dhingra, S., Chopade, P. M., Vinnakota, R. & Kumar, J. Functional implications of the
1022 exon 9 splice insert in GluK1 kainate receptors. *Elife* **12** (2024).
1023 https://doi.org:10.7554/eLife.89755

1024 40 Schauder, D. M. *et al.* Glutamate receptor desensitization is mediated by changes in
1025 quaternary structure of the ligand binding domain. *Proc Natl Acad Sci U S A* **110**, 5921-
1026 5926 (2013). https://doi.org:10.1073/pnas.1217549110

1027 41 Coombs, I. D. *et al.* Homomeric GluA2(R) AMPA receptors can conduct when
1028 desensitized. *Nat Commun* **10**, 4312 (2019). https://doi.org:10.1038/s41467-019-12280-9

1029 42 Twomey, E. C., Yelshanskaya, M. V., Grassucci, R. A., Frank, J. & Sobolevsky, A. I.
1030 Channel opening and gating mechanism in AMPA-subtype glutamate receptors. *Nature*
1031 **549**, 60-65 (2017). https://doi.org:10.1038/nature23479

1032 43 Yelshanskaya, M. V., Patel, D. S., Kottke, C. M., Kurnikova, M. G. & Sobolevsky, A. I.
1033 Opening of glutamate receptor channel to subconductance levels. *Nature* **605**, 172-178
1034 (2022). https://doi.org:10.1038/s41586-022-04637-w

1035 44 Chen, S. *et al.* Activation and Desensitization Mechanism of AMPA Receptor-TARP
1036 Complex by Cryo-EM. *Cell* **170**, 1234-1246.e1214 (2017).
1037 https://doi.org:10.1016/j.cell.2017.07.045

1038 45 Waterhouse, A. *et al.* SWISS-MODEL: homology modelling of protein structures and
1039 complexes. *Nucleic Acids Res* **46**, W296-w303 (2018). https://doi.org:10.1093/nar/gky427

1040 46 Bienert, S. *et al.* The SWISS-MODEL Repository-new features and functionality. *Nucleic*
1041 *Acids Res* **45**, D313-d319 (2017). https://doi.org:10.1093/nar/gkw1132

1042 47 Guex, N., Peitsch, M. C. & Schwede, T. Automated comparative protein structure
1043 modeling with SWISS-MODEL and Swiss-PdbViewer: a historical perspective.
1044 *Electrophoresis* **30 Suppl 1**, S162-173 (2009). https://doi.org:10.1002/elps.200900140

1045 48 Studer, G. *et al.* QMEANDisCo-distance constraints applied on model quality estimation.
1046 *Bioinformatics* **36**, 1765-1771 (2020). https://doi.org:10.1093/bioinformatics/btz828

1047 49 Bertoni, M., Kiefer, F., Biasini, M., Bordoli, L. & Schwede, T. Modeling protein quaternary
1048 structure of homo- and hetero-oligomers beyond binary interactions by homology. *Sci Rep*
1049 **7**, 10480 (2017). https://doi.org:10.1038/s41598-017-09654-8

1050 50 Esmenjaud, J. B. *et al.* An inter-dimer allosteric switch controls NMDA receptor activity.
1051 *Embo j* **38** (2019). https://doi.org:10.15252/embj.201899894

1052 51 Salazar, H., Eibl, C., Chebli, M. & Plested, A. Mechanism of partial agonism in AMPA-type
1053 glutamate receptors. *Nat Commun* **8**, 14327 (2017).
1054 https://doi.org:10.1038/ncomms14327

1055 52 Baranovic, J. & Plested, A. J. Auxiliary subunits keep AMPA receptors compact during
1056 activation and desensitization. *Elife* **7** (2018). https://doi.org:10.7554/eLife.40548

1057 53 Plested, A. J. & Mayer, M. L. AMPA receptor ligand binding domain mobility revealed by
1058 functional cross linking. *J Neurosci* **29**, 11912-11923 (2009).
1059 https://doi.org:10.1523/jneurosci.2971-09.2009

1060 54 Daniels, B. A., Andrews, E. D., Aurousseau, M. R., Accardi, M. V. & Bowie, D. Crosslinking
1061 the ligand-binding domain dimer interface locks kainate receptors out of the main open
1062 state. *J Physiol* **591**, 3873-3885 (2013). https://doi.org:10.1113/jphysiol.2013.253666

1063 55 Careaga, C. L. & Falke, J. J. Thermal motions of surface alpha-helices in the D-galactose
1064 chemosensory receptor. Detection by disulfide trapping. *J Mol Biol* **226**, 1219-1235 (1992).
1065 https://doi.org:10.1016/0022-2836(92)91063-u

1066 56 Larsen, A. P. *et al.* Identification and Structure-Function Study of Positive Allosteric
1067 Modulators of Kainate Receptors. *Mol Pharmacol* **91**, 576-585 (2017).
1068 https://doi.org:10.1124/mol.116.107599

1069 57 Bay, Y. *et al.* The positive allosteric modulator BPAM344 and L-glutamate introduce an
1070 active-like structure of the ligand-binding domain of GluK2. *FEBS Lett* **598**, 743-757 (2024).
1071 https://doi.org:10.1002/1873-3468.14824

1072 58 Twomey, E. C. & Sobolevsky, A. I. Structural Mechanisms of Gating in Ionotropic
1073 Glutamate Receptors. *Biochemistry* **57**, 267-276 (2018).
1074 https://doi.org:10.1021/acs.biochem.7b00891

1075 59 Zhou, C. & Tajima, N. Structural insights into NMDA receptor pharmacology. *Biochem Soc*
1076 *Trans* **51**, 1713-1731 (2023). https://doi.org:10.1042/bst20230122

1077 60 Klein, R. M. & Howe, J. R. Effects of the lurcher mutation on GluR1 desensitization and
1078 activation kinetics. *J Neurosci* **24**, 4941-4951 (2004).
1079 https://doi.org:10.1523/jneurosci.0660-04.2004

1080 61 Wilding, T. J. & Huettner, J. E. Cadmium opens GluK2 kainate receptors with cysteine
1081 substitutions at the M3 helix bundle crossing. *J Gen Physiol* **151**, 435-451 (2019).
1082 https://doi.org:10.1085/jgp.201812234

1083 62 Fleck, M. W., Cornell, E. & Mah, S. J. Amino-acid residues involved in glutamate receptor
1084 6 kainate receptor gating and desensitization. *J Neurosci* **23**, 1219-1227 (2003).
1085 https://doi.org:10.1523/jneurosci.23-04-01219.2003

1086 63 Twomey, E. C., Yelshanskaya, M. V., Grassucci, R. A., Frank, J. & Sobolevsky, A. I.
1087 Structural Bases of Desensitization in AMPA Receptor-Auxiliary Subunit Complexes.
1088 *Neuron* **94**, 569-580.e565 (2017). https://doi.org:10.1016/j.neuron.2017.04.025

1089 64 Klykov, O., Gangwar, S. P., Yelshanskaya, M. V., Yen, L. & Sobolevsky, A. I. Structure
1090 and desensitization of AMPA receptor complexes with type II TARP γ5 and GSG1L. *Mol*
1091 *Cell* **81**, 4771-4783.e4777 (2021). https://doi.org:10.1016/j.molcel.2021.09.030

1092 65 Herguedas, B. *et al.* Mechanisms underlying TARP modulation of the GluA1/2-γ8 AMPA
1093 receptor. *Nat Commun* **13**, 734 (2022). https://doi.org:10.1038/s41467-022-28404-7

1094 66 Gangwar, S. P. *et al.* Modulation of GluA2-γ5 synaptic complex desensitization, polyamine
1095 block and antiepileptic perampanel inhibition by auxiliary subunit cornichon-2. *Nat Struct*
1096 *Mol Biol* **30**, 1481-1494 (2023). https://doi.org:10.1038/s41594-023-01080-x

1097 67 Reiner, A. & Isacoff, E. Y. Tethered ligands reveal glutamate receptor desensitization
1098 depends on subunit occupancy. *Nat Chem Biol* **10**, 273-280 (2014).
1099 https://doi.org:10.1038/nchembio.1458

1100 68 Fisher, M. T. & Fisher, J. L. Contributions of different kainate receptor subunits to the
1101 properties of recombinant homomeric and heteromeric receptors. *Neuroscience* **278**, 70-
1102 80 (2014). https://doi.org:10.1016/j.neuroscience.2014.08.009

1103 69 Salazar, H., Mischke, S. & Plested, A. J. R. Measurements of the Timescale and
1104 Conformational Space of AMPA Receptor Desensitization. *Biophys J* **119**, 206-218 (2020).
1105 https://doi.org:10.1016/j.bpj.2020.05.029

1106 70 Zhang, D. *et al.* Structural mobility tunes signalling of the GluA1 AMPA glutamate receptor.
1107 *Nature* **621**, 877-882 (2023). https://doi.org:10.1038/s41586-023-06528-0

1108 71 Larsen, A. H., Perozzo, A. M., Biggin, P. C., Bowie, D. & Kastrup, J. S. Recovery from
1109 desensitization in GluA2 AMPA receptors is affected by a single mutation in the N-terminal
1110 domain interface. *J Biol Chem* **300**, 105717 (2024).
1111 https://doi.org:10.1016/j.jbc.2024.105717

1112 72 Zhang, W. *et al.* A transmembrane accessory subunit that modulates kainate-type
1113 glutamate receptors. *Neuron* **61**, 385-396 (2009).
1114 https://doi.org:10.1016/j.neuron.2008.12.014

1115 73 Swanson, G. T., Feldmeyer, D., Kaneda, M. & Cull-Candy, S. G. Effect of RNA editing and
1116 subunit co-assembly single-channel properties of recombinant kainate receptors. *J*
1117 *Physiol* **492 (Pt 1)**, 129-142 (1996). https://doi.org:10.1113/jphysiol.1996.sp021295

1118 74 Aittoniemi, J., Jensen, M., Pan, A. C. & Shaw, D. E. Desensitization dynamics of the AMPA
1119 receptor. *Structure* **31**, 724-734.e723 (2023). https://doi.org:10.1016/j.str.2023.03.013

1120 75 Carbone, A. L. & Plested, A. J. Coupled control of desensitization and gating by the ligand
1121 binding domain of glutamate receptors. *Neuron* **74**, 845-857 (2012).
1122 https://doi.org:10.1016/j.neuron.2012.04.020

1123 76 Plested, A. J. & Mayer, M. L. Structure and mechanism of kainate receptor modulation by
1124 anions. *Neuron* **53**, 829-841 (2007). https://doi.org:10.1016/j.neuron.2007.02.025

1125 77 Dürr, K. L. *et al.* Structure and dynamics of AMPA receptor GluA2 in resting, pre-open,
1126 and desensitized states. *Cell* **158**, 778-792 (2014).
1127 https://doi.org:10.1016/j.cell.2014.07.023

1128 78 Ivica, J. *et al.* Proton-triggered rearrangement of the AMPA receptor N-terminal domains
1129 impacts receptor kinetics and synaptic localization. *Nat Struct Mol Biol* **31**, 1601-1613
1130 (2024). https://doi.org:10.1038/s41594-024-01369-5

1131 79 Revah, F. *et al.* Mutations in the channel domain alter desensitization of a neuronal
1132 nicotinic receptor. *Nature* **353**, 846-849 (1991). https://doi.org:10.1038/353846a0

1133 80 Bowie, D. & Lange, G. D. Functional stoichiometry of glutamate receptor desensitization.
1134 *J Neurosci* **22**, 3392-3403 (2002). https://doi.org:10.1523/jneurosci.22-09-03392.2002

1135 81 Dawe, G. B. *et al.* Defining the structural relationship between kainate-receptor
1136 deactivation and desensitization. *Nat Struct Mol Biol* **20**, 1054-1061 (2013).
1137 https://doi.org:10.1038/nsmb.2654

1138

1139

1140

1141

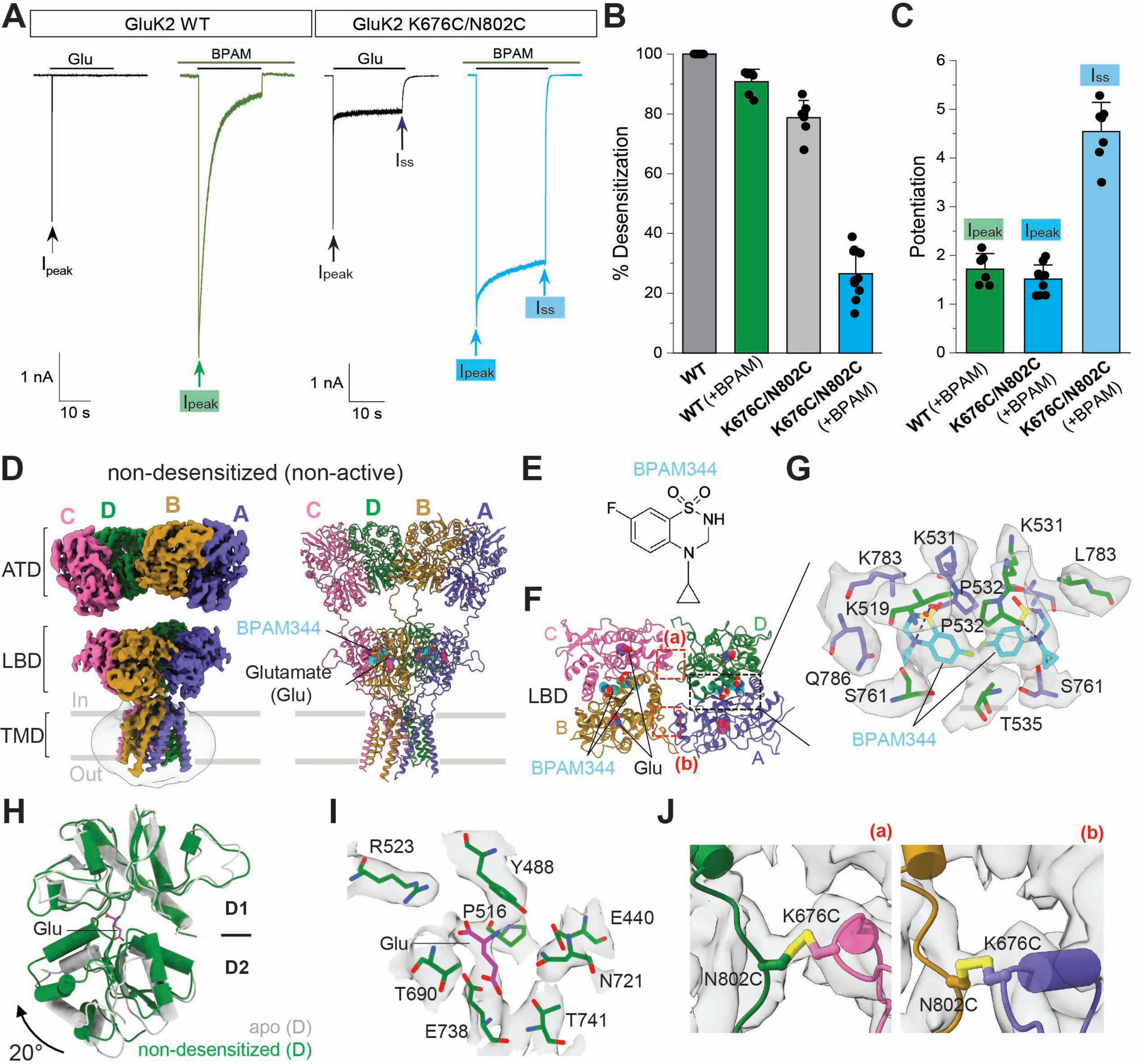
A
GluK2 WT
GluK2 K676C/N802C
Glu
BPAM
Ipeak
Iss
1 nA
10 s
B
% Desensitization
WT
WT (+BPAM)
K676C/N802C
K676C/N802C (+BPAM)
C
Potentiation
D
non-desensitized (non-active)
ATD
LBD
TMD
In
Out
BPAM344
Glutamate (Glu)
E
F
(a)
(b)
G
K783
K531
L783
K519
P532
Q786
S761
T535
H
D1
D2
apo (D)
non-desensitized (D)
20°
I
R523
Y488
P516
E440
N721
T690
T741
E738
J
K676C
N802C

Figure 1

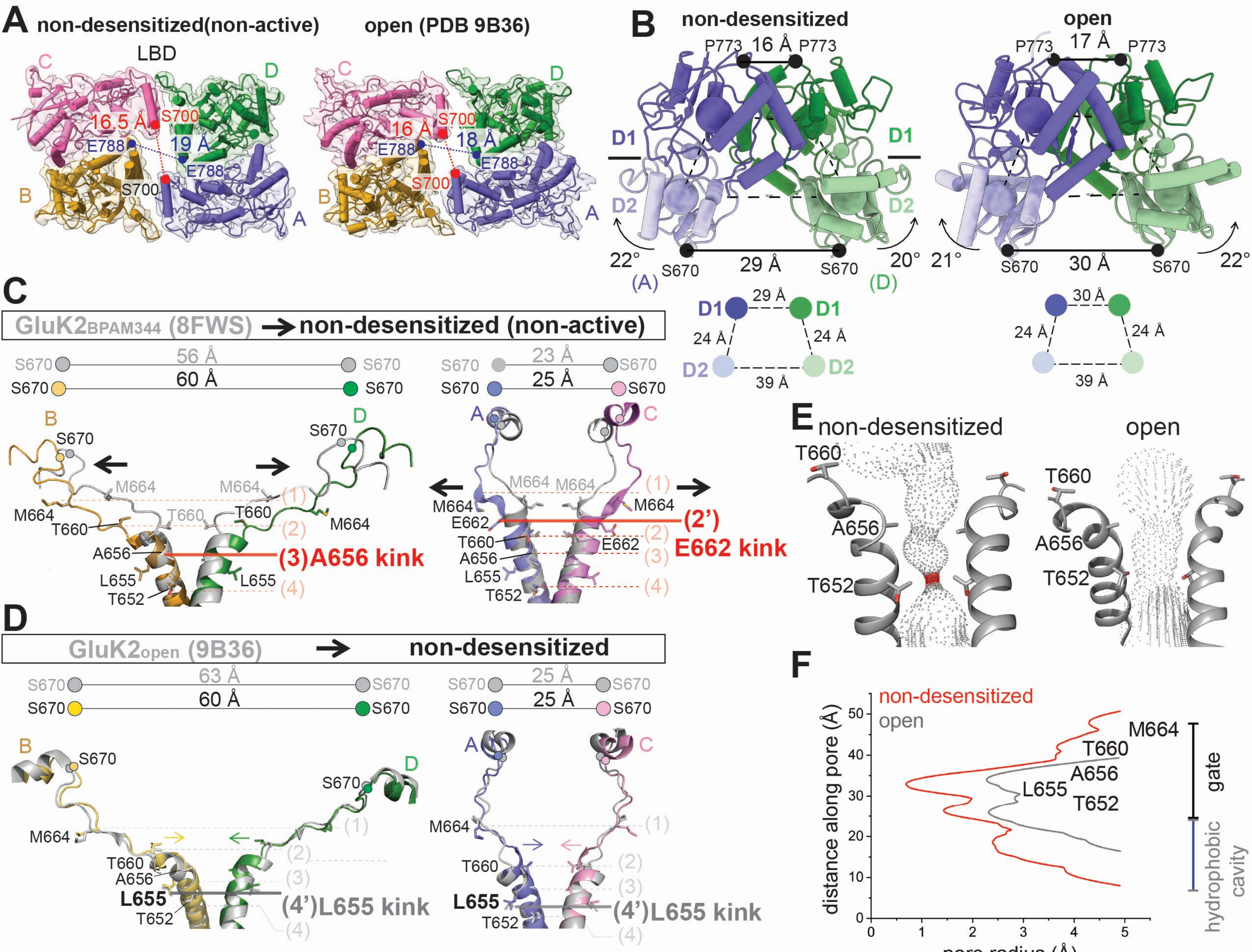
A
non-desensitized(non-active)
open (PDB 9B36)
LBD
C
D
B
A
16.5 Å
S700
E788
19 Å
16 Å
18 Å
B
non-desensitized
open
P773
16 Å
17 Å
D1
D2
22°
20°
21°
S670
29 Å
30 Å
(A)
(D)
24 Å
39 Å
C
GluK2BPAM344 (8FWS) → non-desensitized (non-active)
56 Å
60 Å
23 Å
25 Å
M664
T660
A656
L655
T652
E662
(1)
(2)
(3)A656 kink
(2')
E662 kink
(3)
(4)
D
GluK2open (9B36) → non-desensitized
63 Å
60 Å
25 Å
25 Å
(4')L655 kink
E
non-desensitized
open
T660
A656
T652
F
non-desensitized
open
distance along pore (Å)
pore radius (Å)
M664
T660
A656
L655
T652
gate
hydrophobic cavity

Figure 2

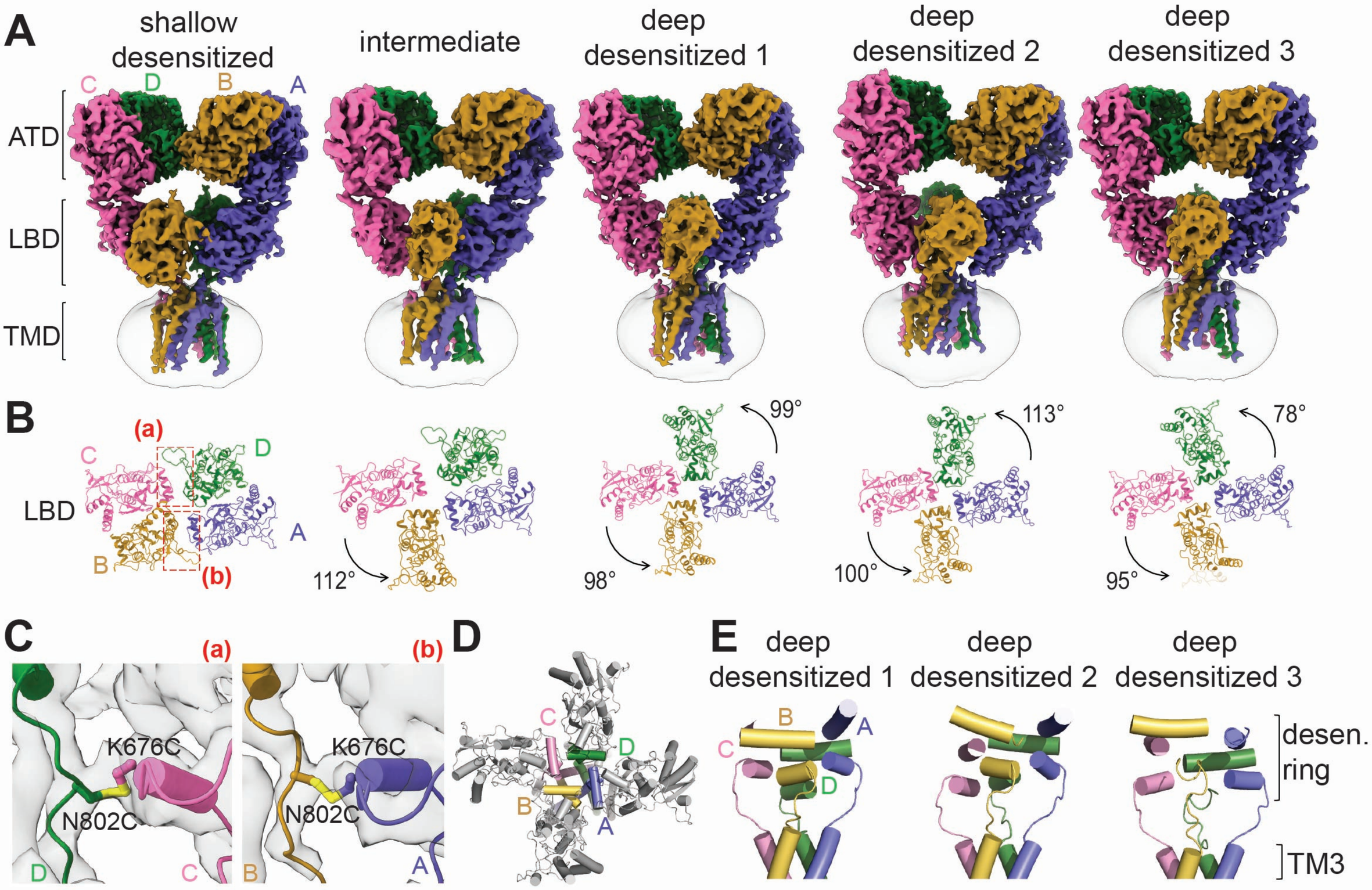
A
shallow desensitized
intermediate
deep desensitized 1
deep desensitized 2
deep desensitized 3
C
D
B
A
ATD
LBD
TMD
B
(a)
(b)
LBD
112°
98°
99°
100°
113°
95°
78°
C
K676C
N802C
D
E
desen. ring
TM3

Figure 3

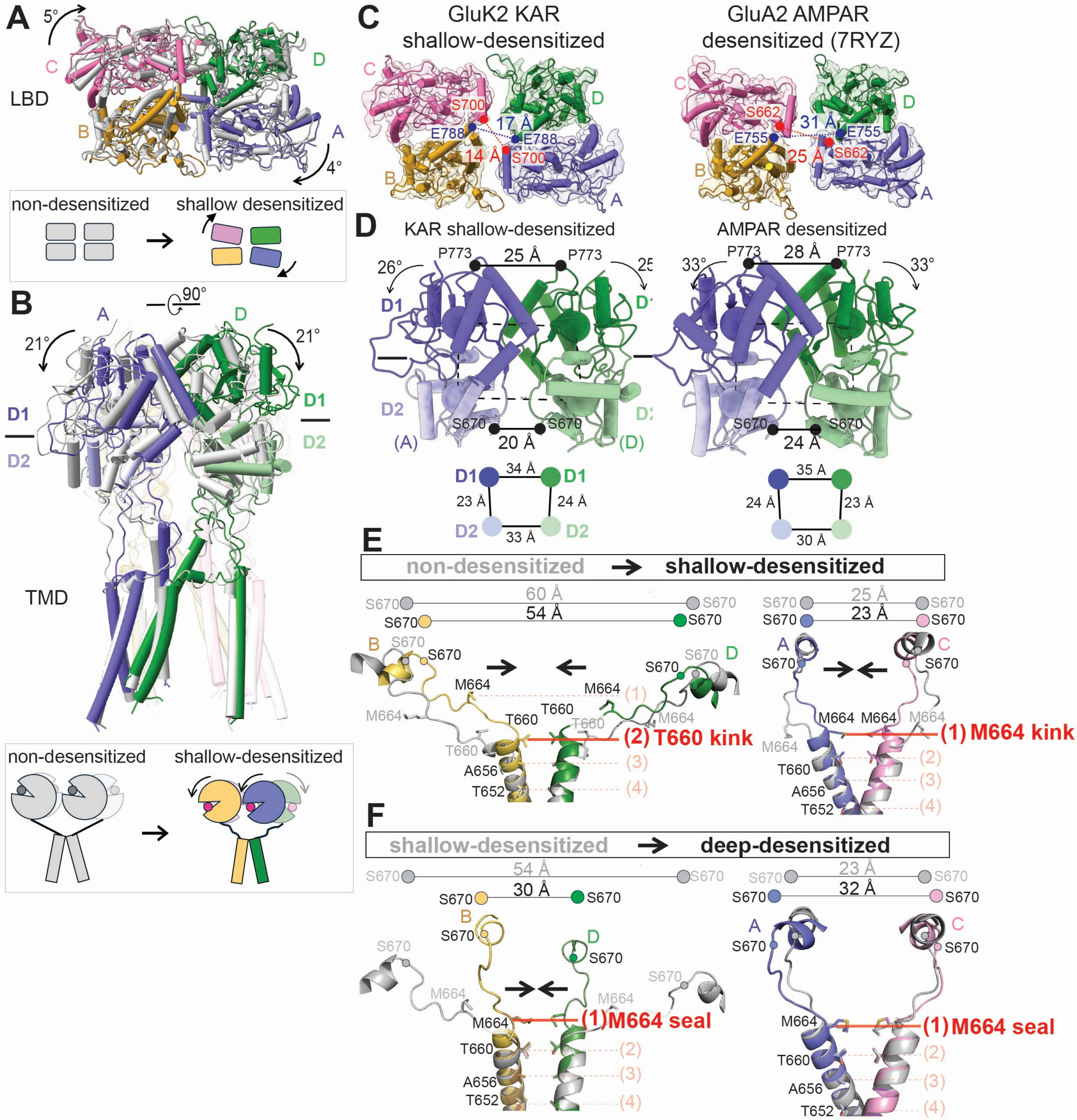
A
5°
C
D
LBD
B
A
4°
non-desensitized
shallow desensitized
B
90°
A
D
21°
21°
D1
D1
D2
D2
TMD
non-desensitized
shallow-desensitized
C
GluK2 KAR
shallow-desensitized
GluA2 AMPAR
desensitized (7RYZ)
S700
17 Å
E788
E788
14 Å
S700
S662
31 Å
E755
E755
25 Å
S662
D
KAR shallow-desensitized
AMPAR desensitized
P773
25 Å
P773
26°
P773
28 Å
P773
33°
33°
D1
D2
S670
S670
20 Å
(A)
(D)
S670
S670
24 Å
D1
34 Å
D1
23 Å
24 Å
D2
33 Å
D2
35 A
24 Å
23 Å
30 Å
E
non-desensitized
shallow-desensitized
60 Å
54 Å
S670
S670
B
M664
T660
T660
T660
M664
M664
(1)
(2) T660 kink
(3)
(4)
A656
T652
25 Å
23 Å
A
C
M664
M664
M664
(1) M664 kink
(2)
(3)
(4)
F
shallow-desensitized
deep-desensitized
54 Å
30 Å
23 Å
32 Å
S670
B
D
M664
M664
(1) M664 seal
T660
(2)
(3)
A656
T652
(4)
A
C
M664
(1) M664 seal
T660
(2)
(3)
A656
T652
(4)

Figure 4

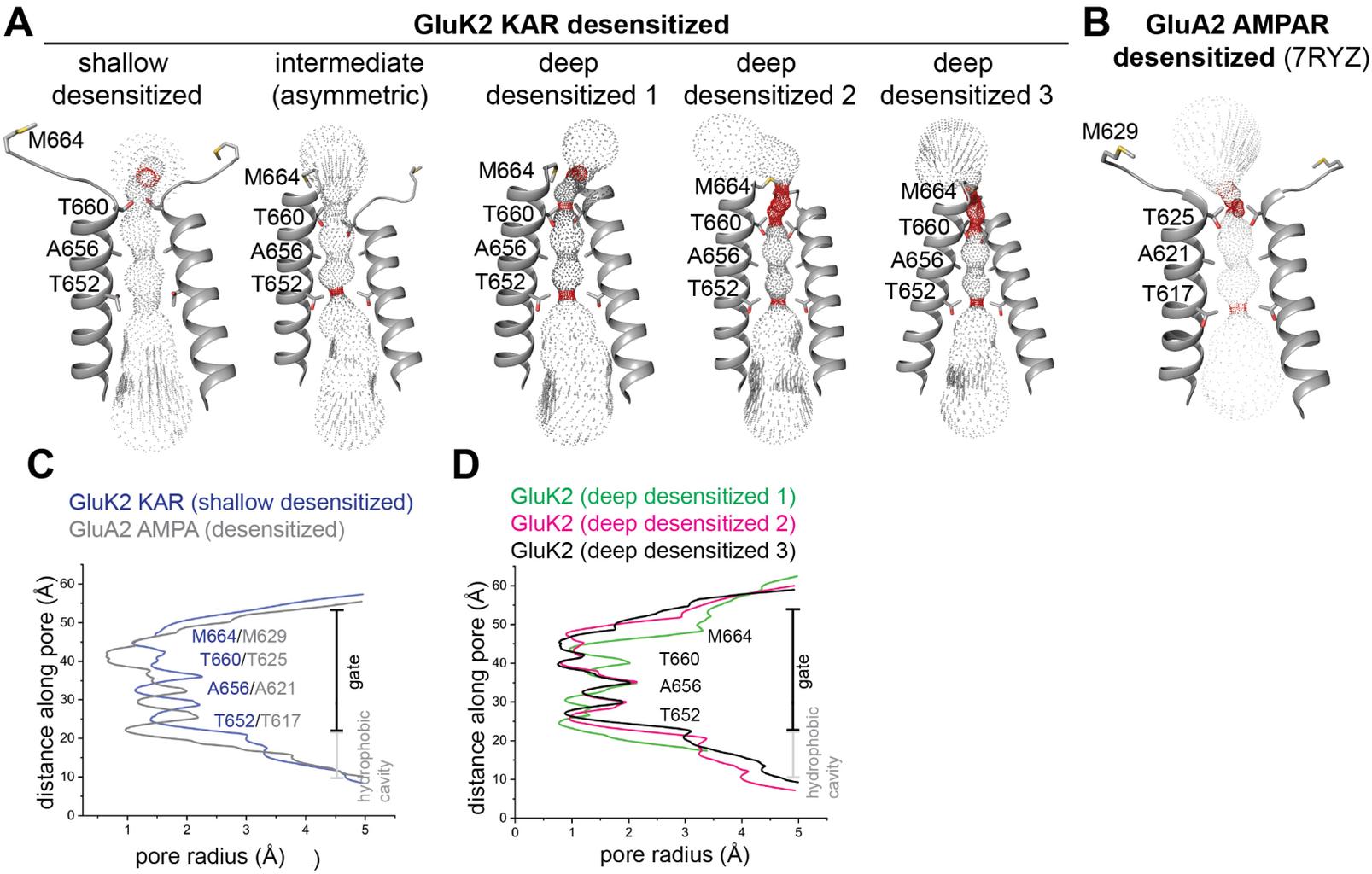
A
GluK2 KAR desensitized
shallow desensitized
intermediate (asymmetric)
deep desensitized 1
deep desensitized 2
deep desensitized 3
M664
T660
A656
T652
B
GluA2 AMPAR desensitized (7RYZ)
M629
T625
A621
T617
C
GluK2 KAR (shallow desensitized)
GluA2 AMPA (desensitized)
M664/M629
T660/T625
A656/A621
T652/T617
gate
hydrophobic cavity
distance along pore (Å)
pore radius (Å)
D
GluK2 (deep desensitized 1)
GluK2 (deep desensitized 2)
GluK2 (deep desensitized 3)
M664
T660
A656
T652
gate
hydrophobic cavity
distance along pore (Å)
pore radius (Å)

Figure 5

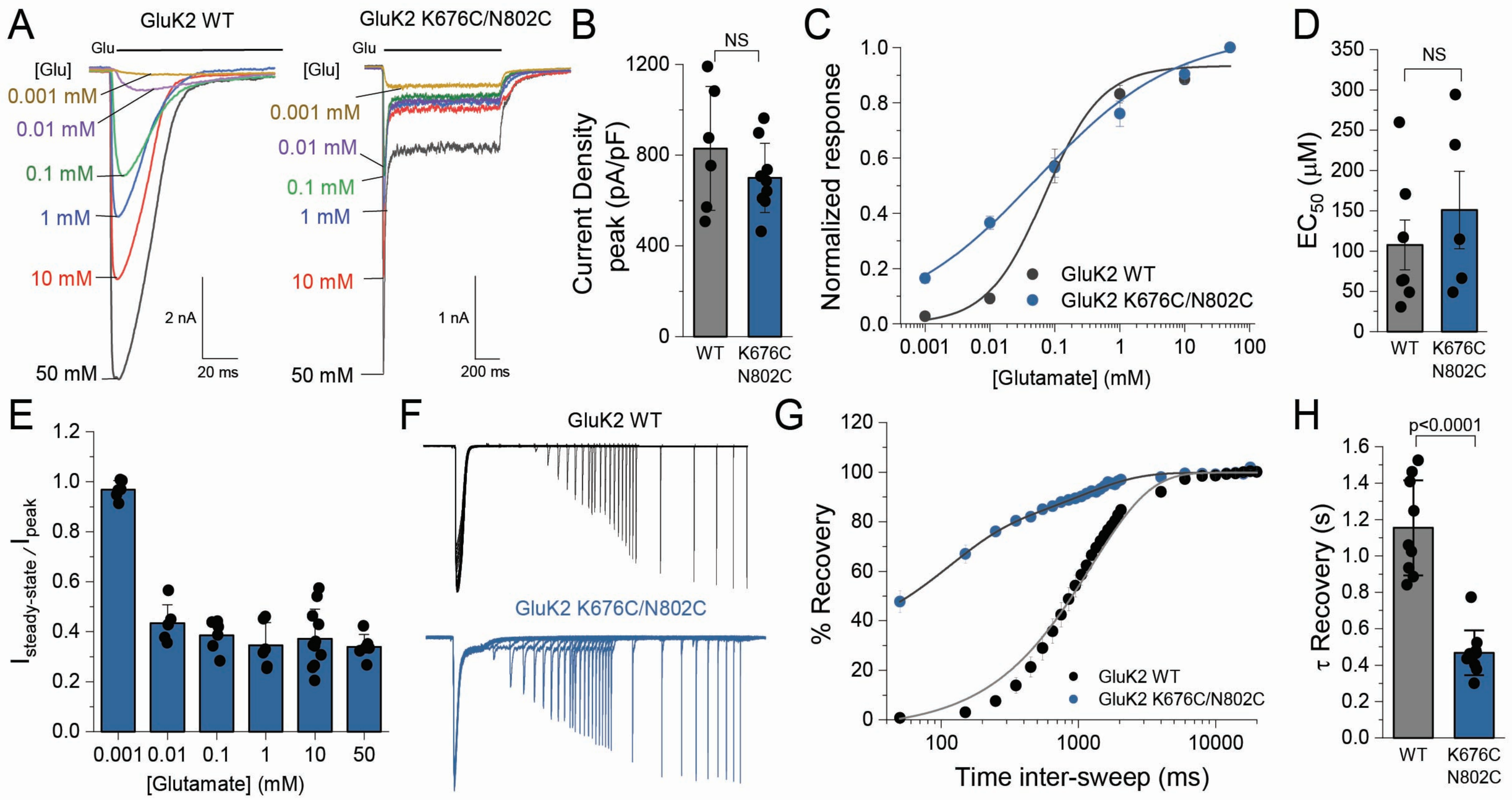
A
GluK2 WT
GluK2 K676C/N802C
Glu
[Glu]
0.001 mM
0.01 mM
0.1 mM
1 mM
10 mM
50 mM
2 nA
20 ms
1 nA
200 ms
B
NS
Current Density peak (pA/pF)
WT
K676C N802C
C
Normalized response
[Glutamate] (mM)
GluK2 WT
GluK2 K676C/N802C
D
NS
EC50 (µM)
WT
K676C N802C
E
Isteady-state / Ipeak
[Glutamate] (mM)
F
GluK2 WT
GluK2 K676C/N802C
G
% Recovery
Time inter-sweep (ms)
GluK2 WT
GluK2 K676C/N802C
H
p<0.0001
τ Recovery (s)
WT
K676C N802C

Figure 6

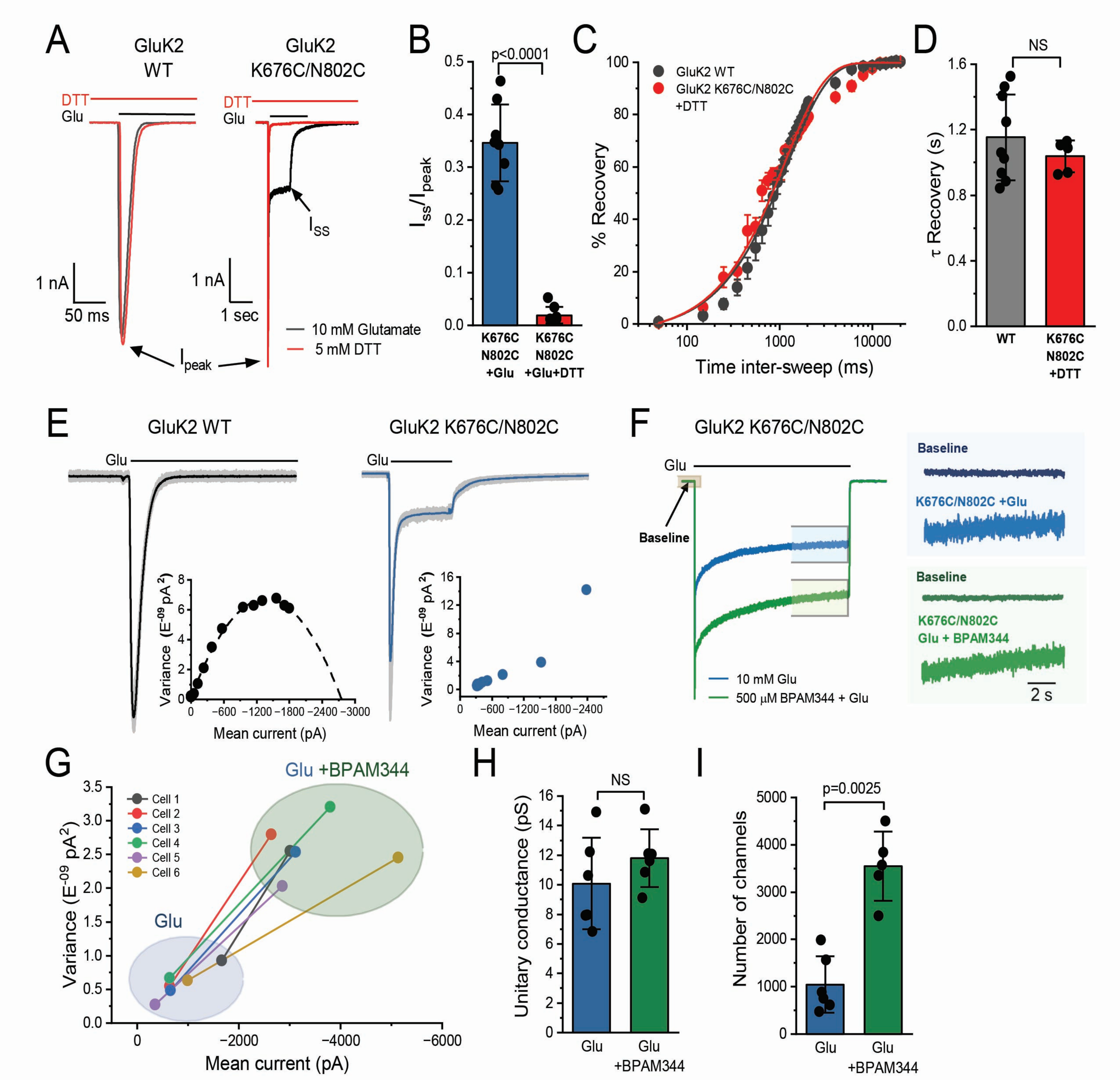
A
GluK2 WT
GluK2 K676C/N802C
DTT
Glu
1 nA
50 ms
1 sec
I_{peak}
I_{SS}
10 mM Glutamate
5 mM DTT
B
p<0.0001
I_{ss}/I_{peak}
K676C N802C +Glu
K676C N802C +Glu+DTT
C
GluK2 WT
GluK2 K676C/N802C +DTT
% Recovery
Time inter-sweep (ms)
D
NS
τ Recovery (s)
WT
K676C N802C +DTT
E
GluK2 WT
GluK2 K676C/N802C
Variance (E^{-09} pA^2)
Mean current (pA)
F
GluK2 K676C/N802C
Baseline
10 mM Glu
500 μM BPAM344 + Glu
K676C/N802C +Glu
K676C/N802C Glu + BPAM344
2 s
G
Glu +BPAM344
Glu
Cell 1
Cell 2
Cell 3
Cell 4
Cell 5
Cell 6
Variance (E^{-09} pA^2)
Mean current (pA)
H
NS
Unitary conductance (pS)
Glu
Glu +BPAM344
I
p=0.0025
Number of channels
Glu
Glu +BPAM344

Figure 7

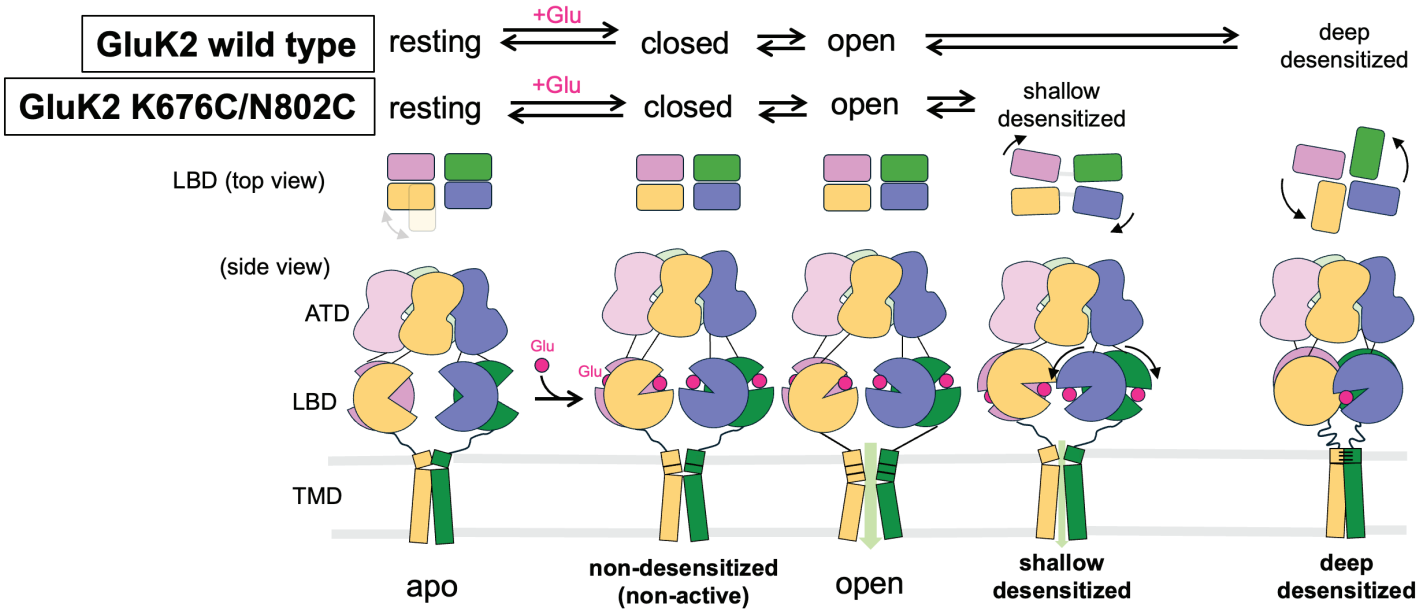
GluK2 wild type
resting
+Glu
closed
open
deep desensitized
GluK2 K676C/N802C
resting
+Glu
closed
open
shallow desensitized
LBD (top view)
(side view)
ATD
LBD
TMD
Glu
Glu
apo
non-desensitized (non-active)
open
shallow desensitized
deep desensitized

Figure 8